

# Quasi-Sterile Neutrinos from Dark Sectors

## I. BSM matter effects in neutrino oscillations and the short-baseline anomalies

---

Daniele S. M. Alves,<sup>a,1</sup> William C. Louis<sup>b</sup> and Patrick G. deNiverville<sup>a</sup>

<sup>a</sup>*Theoretical Division, Los Alamos National Laboratory,  
Los Alamos, NM 87545, U.S.A.*

<sup>b</sup>*Physics Division, Los Alamos National Laboratory,  
Los Alamos, NM 87545, U.S.A.*

*E-mail:* [spier@lanl.gov](mailto:spier@lanl.gov), [louis@lanl.gov](mailto:louis@lanl.gov), [pgdeniverville@lanl.gov](mailto:pgdeniverville@lanl.gov)

**ABSTRACT:** Quasi-sterile neutrinos are a natural consequence of dark sectors interacting with the Standard Model (SM) sector via neutrino- and vector-portals. Essentially, quasi-sterile neutrinos are light dark sector fermions with two generic properties: (i) they mix with the active neutrinos of the SM, and (ii) they are charged under a vector mediator that couples feebly to SM matter. Various interesting phenomenological consequences result from this class of particles. In this article, we investigate one such consequence: new, beyond the SM matter effects that can alter in-medium neutrino oscillations. In particular, for special windows of energy and matter densities, active neutrinos can resonantly oscillate into sterile neutrinos. We take advantage of this feature to build a quasi-sterile neutrino model that can explain the MiniBooNE and LSND anomalies, while remaining compatible with observations from long-baseline reactor- and accelerator-based neutrino experiments. This model is also likely compatible with the recent results reported by the MicroBooNE collaboration (albeit we cannot precisely quantify this claim due to a lack of information in MicroBooNE's public data releases to date). Implications for solar neutrinos and  $\nu_e$  disappearance searches are also briefly discussed.

---

<sup>1</sup>Corresponding author.

---

## Contents

<b>1</b>	<b>Introduction</b>	<b>1</b>
<b>2</b>	<b>The minimal case as a toy model</b>	<b>3</b>
2.1	Neutrino propagation eigenstates in three energy regimes	8
2.2	Neutrino oscillation probabilities	10
2.3	Matter effects on antineutrinos	14
<b>3</b>	<b>Beyond the minimal model: a viable explanation for the MiniBooNE excess</b>	<b>16</b>
3.1	Full Model — Part I: the triple-resonance mechanism	18
3.1.1	Accelerator constraints on the triple-resonance mechanism	19
3.1.2	Reactor constraints on the triple-resonance mechanism	20
3.2	Full Model — Part II: the ‘vanilla’ off-resonance component	21
3.3	Full Model — Part III: fitting the MiniBooNE low energy excess	23
<b>4</b>	<b>Further implications of quasi-sterile neutrinos and BSM matter effects</b>	<b>25</b>
4.1	Implications for MicroBooNE	26
4.2	Implications for solar neutrinos	30
<b>5</b>	<b>Summary and Outlook</b>	<b>31</b>

---

## 1 Introduction

Over the past decade, light dark sectors have emerged as a contender to the WIMP paradigm in providing a possible explanation for the cosmological origin and particle nature of dark matter [1–5]. While there is no consensus on a precise definition of dark sectors, a fairly generic framework to characterize their phenomenology are the so-called *portals*: particle ‘mediators’ that couple to matter and/or forces both in the Standard Model (SM) and in the dark sector, typically (but not necessarily) by mixing with neutral SM particles—such as the photon, the Higgs boson, or neutrinos—if their quantum numbers permit. Most dark sector phenomenological studies, however, take the approach of ‘switching on’ only one individual portal at a time. In this article, we investigate a broader scenario of two simultaneous dark sectors portals, namely, the *neutrino* and *vector* portals, and focus on one generic phenomenological consequence: *quasi-sterile neutrinos*. Specifically, the neutrino portal can be realized by light (say, sub-keV) dark sector fermions mixing with the active neutrinos of the Standard Model. Since these dark sector fermions are neutral under the SM gauge interactions, they are, by definition, *sterile neutrinos*. However, in the presence

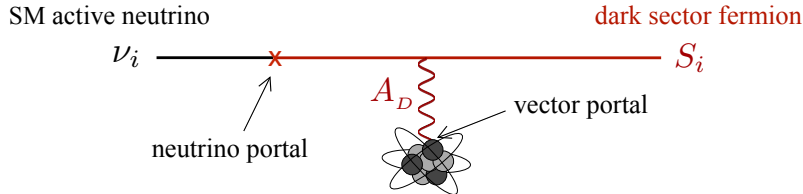


**Figure 1.** A generic consequence of dark sectors with neutrino- and vector-ports are quasi-sterile neutrinos. The BSM matter potential generated by the dark vector interactions can alter neutrino oscillations in matter.

of a vector portal—a dark sector gauge interaction that couples feebly to SM fermions—sterile neutrinos charged under the vector portal might be more appropriately characterized as *quasi*-sterile neutrinos (see Fig. 1). From this, two phenomenological features naturally arise: (i) the presence of beyond the Standard Model (BSM) neutrino oscillations due to mixing of active and sterile neutrinos, and (ii) the possibility of BSM matter effects, and therefore, of *resonant* active-to-sterile neutrino oscillations for specific regimes of matter density and neutrino energy.

There are many interesting motivations to study quasi-sterile neutrinos. One of them is the excess of electron recoil events recently reported by the XENON1T collaboration [6]. Attempts to explain this excess as a signal of solar neutrinos scattering off electrons via an anomalous neutrino magnetic dipole moment are in tension with limits from stellar cooling [7–10]. On the other hand, these astrophysical constraints could be relaxed if the anomalous XENON1T electron recoil events were instead induced by quasi-sterile solar neutrinos scattering via a light dark mediator (see also [11–14]). This topic will be explored in a future publication [15].

Another motivation for quasi-sterile neutrinos, which will be the focus of this article, is the puzzle posed by the short-baseline neutrino oscillation anomalies, which could be an indication of light sterile states mixing with the active neutrinos of the SM. Two intriguing anomalies of this type are the  $\bar{\nu}_\mu \rightarrow \bar{\nu}_e$  and  $\nu_\mu \rightarrow \nu_e$  appearance events reported by the LSND [16–20] and MiniBooNE [21, 22] collaborations. The data in both of these experiments show excesses of (anti-)electron-neutrino charged-current events at  $L/E_\nu \sim 0.5 - 2$  m/MeV, at rates compatible with  $\bar{\nu}_e$  appearance probabilities of  $O(0.1-1\%)$ . These  $\bar{\nu}_e$  appearance events cannot be accommodated in the SM description of neutrino masses and mixings. A simple BSM model including one sterile neutrino species in addition to the three active species (the ‘vanilla’ 3+1 model) can provide a good fit to the LSND excess, the MiniBooNE excess in *antineutrino* mode, and the MiniBooNE excess in *neutrino* mode for the energy range  $E_\nu \gtrsim 400$  MeV. However, an excess of  $\nu_e$  appearance events with lower energies  $E_\nu \sim 150 - 300$  MeV still persists in the MiniBooNE data which cannot be satisfactorily explained by any ‘3+n’ sterile neutrino model<sup>1</sup> [28–36]. This challenge has led to numerous attempts to explain the MiniBooNE low energy excess by invoking new physics of a dark

<sup>1</sup>Recent results from the MicroBooNE collaboration [23] further disfavor the interpretation of the MiniBooNE low energy excess as due to single photon backgrounds from radiative  $\Delta$  decays [24–28].

sector. In the ‘non-oscillatory’ approaches [37–52], production and decays of dark sector fermions and/or light bosons yield final states with  $\nu_e$ ,  $\gamma$ , or collimated  $e^+e^-$  pairs in the MiniBooNE detector, all of which could potentially mimic a  $\nu_e$  charged-current scattering event. In the ‘oscillatory’ approaches, BSM effects alter neutrino propagation through a medium (either ordinary matter [53], the C $\nu$ B [54], or extra dimensions [55, 56]), leading to resonant neutrino oscillations within the window of energy where the MiniBooNE low energy excess is concentrated. Previous attempts to implement oscillatory approaches have not been successful, however, because new matter effects invariably alter the effective in-medium mass splittings of active neutrinos [57–60], leading to oscillation probabilities incompatible with observations at long-baseline neutrino experiments.

In this article, we show that these difficulties can be overcome by a ‘triple-resonance mechanism’ that is able to preserve the in-medium active neutrino mass spectrum at high energies probed by accelerator based-neutrino experiments, as well as the in-medium antineutrino mass spectrum at low energies probed by reactor-based experiments.

At this point it is incumbent on us to comment on the recent  $\nu_e$  searches by the MicroBooNE experiment based on data obtained from an exposure of  $7 \times 10^{20}$  protons-on-target (POT) from the Booster Neutrino Beam (BNB) [61]. These analyses appear to strongly disfavor the hypothesis that the MiniBooNE low energy excess is due to  $\nu_e$  scattering events. As we shall discuss in Subsec. 4.1, this conclusion is strongly model dependent and likely does not hold at a high enough confidence level to exclude the ‘oscillatory’ BSM explanation of the MiniBooNE low energy excess proposed in this study.

This article is organized as follows: in Sec. 2, we introduce and dissect the main features of the resonant mechanism in a toy model, which will then be used in Sec. 3 to build a full model explaining the MiniBooNE excess. Sec. 4 considers the full model’s consistency with the recent MicroBooNE results, and provides a brief discussion of implications for solar neutrinos. Sec. 5 summarizes this article’s main points and provides an outlook of future experimental measurements that could falsify the quasi-sterile neutrino explanation of short-baseline anomalies.

## 2 The minimal case as a toy model

We begin by considering the simplest case of a single quasi-sterile neutrino flavor, which we shall call  $S_3$ , mixing with the active neutrinos of the SM model. It turns out that this minimalistic model does not provide a satisfactory explanation of the short-baseline neutrino anomalies. However, it retains all the basic phenomenological features of the full model to be considered in the next section, and therefore, for pedagogical purposes, we will introduce it first in this section and highlight its key aspects and shortcomings.

We adopt the PDG convention [62] to relate the neutrino mass eigenstates in the SM,  $\nu_i$  ( $i = 1, 2, 3$ ), to the active neutrino flavors,  $\nu_\ell$  ( $\ell = e, \mu, \tau$ ):

$$|\nu_1\rangle = U_{e1} |\nu_e\rangle + U_{\mu 1} |\nu_\mu\rangle + U_{\tau 1} |\nu_\tau\rangle \quad (2.1a)$$

$$|\nu_2\rangle = U_{e2} |\nu_e\rangle + U_{\mu 2} |\nu_\mu\rangle + U_{\tau 2} |\nu_\tau\rangle \quad (2.1b)$$

$$|\nu_3\rangle = U_{e3} |\nu_e\rangle + U_{\mu 3} |\nu_\mu\rangle + U_{\tau 3} |\nu_\tau\rangle \quad (2.1c)$$

where the  $U_{\ell i}$  coefficients above are the matrix elements of the PMNS matrix  $U$ , which is parametrized by three mixing angles  $\theta_{12}$ ,  $\theta_{23}$  and  $\theta_{13}$ , and a CP-violating phase  $\delta_{\text{CP}}$ :

$$U = \begin{pmatrix} 1 & 0 & 0 \\ 0 & c_{23} & s_{23} \\ 0 & -s_{23} & c_{23} \end{pmatrix} \cdot \begin{pmatrix} c_{13} & 0 & s_{13} e^{-i\delta_{\text{CP}}} \\ 0 & 1 & 0 \\ -s_{13} e^{i\delta_{\text{CP}}} & 0 & c_{13} \end{pmatrix} \cdot \begin{pmatrix} c_{12} & s_{12} & 0 \\ -s_{12} & c_{12} & 0 \\ 0 & 0 & 1 \end{pmatrix} \quad (2.2)$$

with  $s_{ij} \equiv \sin \theta_{ij}$  and  $c_{ij} \equiv \cos \theta_{ij}$ .

In this minimal model, we will introduce a small mixing between the sterile neutrino  $S_3$  and one of the active neutrino states, namely,  $\nu_3$ , parametrized by a mixing angle  $\theta_{S_3} \ll 1$ . The mass eigenstates *in vacuum* are given by:

$$|\nu_1\rangle = \sum_{\ell=e,\mu,\tau} U_{\ell 1} |\nu_\ell\rangle \quad (2.3a)$$

$$|\nu_2\rangle = \sum_{\ell=e,\mu,\tau} U_{\ell 2} |\nu_\ell\rangle \quad (2.3b)$$

$$\begin{aligned} |N_{3, \text{vac}}^{(-)}\rangle &= -\sin \theta_{S_3} |S_3\rangle + \cos \theta_{S_3} |\nu_3\rangle \\ &= -\sin \theta_{S_3} |S_3\rangle + \cos \theta_{S_3} \sum_{\ell=e,\mu,\tau} U_{\ell 3} |\nu_\ell\rangle \end{aligned} \quad (2.3c)$$

$$\begin{aligned} |N_{3, \text{vac}}^{(+)}\rangle &= \cos \theta_{S_3} |S_3\rangle + \sin \theta_{S_3} |\nu_3\rangle \\ &= \cos \theta_{S_3} |S_3\rangle + \sin \theta_{S_3} \sum_{\ell=e,\mu,\tau} U_{\ell 3} |\nu_\ell\rangle \end{aligned} \quad (2.3d)$$

with mass eigenvalues  $m_1$ ,  $m_2$ ,  $m_3$ , and  $M_3 \gg m_3$ , respectively. Since  $\sin \theta_{S_3} \ll 1$ , the heavy eigenstate  $N_3^{(+)}$  is mostly sterile with a small active component, whereas  $N_3^{(-)}$  is composed mostly of the active neutrino state  $\nu_3$ , with a small sterile component.

All of the above information can be captured in the neutrino Hamiltonian. Working in the basis  $B = \{|\nu_1\rangle, |\nu_2\rangle, |\nu_3\rangle, |S_3\rangle\}$ , we can write the vacuum Hamiltonian in a familiar form:

$$\begin{aligned} \widehat{H}_{B, \text{vacuum}} &\simeq \begin{pmatrix} 1 & 0 & 0 & 0 \\ 0 & 1 & 0 & 0 \\ 0 & 0 & \cos \theta_{S_3} & \sin \theta_{S_3} \\ 0 & 0 & -\sin \theta_{S_3} & \cos \theta_{S_3} \end{pmatrix} \cdot \begin{pmatrix} \frac{m_1^2}{2E_\nu} & 0 & 0 & 0 \\ 0 & \frac{m_2^2}{2E_\nu} & 0 & 0 \\ 0 & 0 & \frac{m_3^2}{2E_\nu} & 0 \\ 0 & 0 & 0 & \frac{M_3^2}{2E_\nu} \end{pmatrix} \cdot \begin{pmatrix} 1 & 0 & 0 & 0 \\ 0 & 1 & 0 & 0 \\ 0 & 0 & \cos \theta_{S_3} & -\sin \theta_{S_3} \\ 0 & 0 & \sin \theta_{S_3} & \cos \theta_{S_3} \end{pmatrix} \\ &= (\dots) \times \mathbf{1}_{3 \times 3} + \frac{\delta M_3^2}{4E_\nu} \begin{pmatrix} -1 + 2\frac{\delta m_{13}^2}{\delta M_3^2} & 0 & 0 & 0 \\ 0 & -1 + 2\frac{\delta m_{23}^2}{\delta M_3^2} & 0 & 0 \\ 0 & 0 & -\cos 2\theta_{S_3} & \sin 2\theta_{S_3} \\ 0 & 0 & \sin 2\theta_{S_3} & \cos 2\theta_{S_3} \end{pmatrix} \quad (2.4) \end{aligned}$$

where we have defined the mass-squared splittings  $\delta M_3^2 \equiv M_3^2 - m_3^2$ ,  $\delta m_{ij}^2 \equiv m_i^2 - m_j^2$ , and we did not bother to write the terms proportional to the identity operator in the second line

of (2.4), since they do not affect the difference between energy eigenvalues and therefore do not contribute to neutrino oscillations.

When propagating through a medium, neutrinos receive additional contributions to their energies due to the presence of matter potentials (which can be understood as coherent forward scattering at zero momentum transfer). If this effect is felt identically by all neutrino states—which is the case, in the SM, of the matter potential generated by the neutral weak interactions mediated by the  $Z^0$  boson—the relative phases of the neutrino propagation eigenstates are not changed, and therefore such matter potentials do not affect neutrino oscillations in a medium. On the other hand, a matter potential that affects different neutrino flavors non-identically will alter the propagation eigenstates and their relative phases with respect to vacuum, and can lead to significant distortions in neutrino oscillations for certain energy and medium density regimes. The most well-known such effect is due to the charged weak interactions mediated by the  $W^\pm$  bosons, which generate an effective matter potential to the electron-neutrino flavor, but not to muon- nor tau-neutrino flavors, since the only charged leptons present in ordinary matter are electrons. This is known as the standard Mikheyev–Smirnov–Wolfenstein (MSW) effect [63–66].

In the framework of dark sectors, it is only natural to expect that dark gauge bosons might mediate interactions between sterile neutrinos and SM fermions. The interactions with stable SM fermions, specifically, will generate a new matter potential source for neutrinos propagating through matter, and will alter neutrino oscillations as long as the dark gauge boson does not couple universally to all active and sterile neutrino species. As an example, consider such a dark vector mediator  $A_D$  coupling to the following currents:

$$\mathcal{L}_{\text{dark}} \supset -A_D^\mu \left( g_s \bar{S}_3 \frac{\gamma_\mu(1-\gamma_5)}{2} S_3 + \sum_i g_\nu \bar{\nu}_i \frac{\gamma_\mu(1-\gamma_5)}{2} \nu_i + g_e \bar{e} \gamma_\mu e + g_p \bar{p} \gamma_\mu p + g_n \bar{n} \gamma_\mu n + \dots \right), \quad (2.5)$$

where the dots denote unspecified mediator couplings to heavier fermions. The resulting matter potential experienced by (anti-)neutrinos propagating through matter is then given by (see, *e.g.*, [67]):

$$V_{\nu_i}|_{\text{matter}} = -V_{\bar{\nu}_i}|_{\text{matter}} = -\frac{g_\nu}{2m_{A_D}^2} \sum_{f=e,p,n} g_f n_f, \quad (2.6a)$$

$$V_{S_3}|_{\text{matter}} = -V_{\bar{S}_3}|_{\text{matter}} = -\frac{g_s}{2m_{A_D}^2} \sum_{f=e,p,n} g_f n_f. \quad (2.6b)$$

Above,  $m_{A_D}$  is the dark mediator’s mass, and  $n_f$  is the in-medium number density of the SM fermion species  $f$ . It is clear from (2.6) that these  $A_D$ -induced matter potentials are non-zero only if ordinary matter has finite ‘dark charge’ density. The latter requirement rules out the dark photon as a mediator candidate, since ordinary matter is, on average, charge-neutral to a dark photon. In this specific example, the three active neutrinos experience the same matter potential  $V_{\nu_i}$ , and therefore SM neutrino oscillations are unaffected in regimes for which BSM effects can be neglected. However, as long as  $g_s \neq g_\nu$ , the matter potentials

for the sterile and active species will be distinct, and therefore neutrino oscillations will be affected by the relative potential experienced by  $S_3$ :

$$\Delta V|_{\text{matter}} = (V_{S_3} - V_{\nu_i})|_{\text{matter}} = - \frac{(g_s - g_\nu)}{2m_{A_D}^2} \sum_{f=e,p,n} g_f n_f. \quad (2.7)$$

We note that a variety of phenomenological constraints restrict the mass and couplings of the dark mediator. For instance,  $S_3$  in-medium scattering with finite momentum exchange must be sufficiently suppressed, otherwise this would lead to decoherence of  $S_3 - \nu_3$  oscillations [68]. Further, the combinations  $g_p(g_\nu - g_s \sin \theta_{S_3})$ ,  $g_n(g_\nu - g_s \sin \theta_{S_3})$ , and  $g_e(g_\nu - g_s \sin \theta_{S_3})$  are constrained by neutrino-proton, neutrino-neutron, and neutrino-electron scattering, respectively [69–72]. These constraints can be respected for sufficiently small couplings, and, as evident from (2.7), it is possible to simultaneously keep  $\Delta V$  non-negligible if the mediator mass  $m_{A_D}$  is sufficiently light. Numerous other constraints from colliders, beam dumps, fixed targets, meson decays, stellar cooling, anomalous magnetic dipole moments, etc., also apply in different regions of parameter space of (2.5) [73–76]. We will, however, defer these considerations to a future work. For the remainder of this article, we will remain agnostic about the mass and couplings of the dark mediator  $A_D$ , and instead treat the effective matter potential  $\Delta V$  as a free parameter in order to address the MiniBooNE anomaly. A comprehensive study of experimentally viable UV completions of  $V_{\nu_i}$ ,  $V_{S_3}$ , and further signal predictions, will be the focus of an upcoming publication [15].

The effective matter potential (2.7) for  $S_3$  modifies the neutrino Hamiltonian in matter:

$$\widehat{H}_{B, \text{matter}} = \widehat{H}_{B, \text{vacuum}} - \begin{pmatrix} 0 & 0 & 0 & 0 \\ 0 & 0 & 0 & 0 \\ 0 & 0 & 0 & 0 \\ 0 & 0 & 0 & |\Delta V| \end{pmatrix}, \quad (2.8)$$

where we chose the sign of  $\Delta V$  to be negative (positive) for neutrinos (antineutrinos) for reasons that will become clear shortly.

The neutrino propagation eigenstates of  $\widehat{H}_{B, \text{matter}}$  in (2.8) and their eigenvalues  $\omega$  are easily obtained:

$$|N_{1,m}\rangle = |\nu_1\rangle, \quad \omega_1 = \frac{\delta m_{13}^2}{2E_\nu} \quad (2.9a)$$

$$|N_{2,m}\rangle = |\nu_2\rangle, \quad \omega_2 = \frac{\delta m_{23}^2}{2E_\nu} \quad (2.9b)$$

$$|N_{3,m}^{(-)}\rangle = -\sin \theta_{S_3}^{(m)} |S_3\rangle + \cos \theta_{S_3}^{(m)} |\nu_3\rangle, \quad \omega_3^{(-)} = \frac{\delta M_3^2}{4E_\nu} (1 - C_3) - \frac{|\Delta V|}{2} \quad (2.9c)$$

$$|N_{3,m}^{(+)}\rangle = \cos \theta_{S_3}^{(m)} |S_3\rangle + \sin \theta_{S_3}^{(m)} |\nu_3\rangle, \quad \omega_3^{(+)} = \frac{\delta M_3^2}{4E_\nu} (1 + C_3) - \frac{|\Delta V|}{2} \quad (2.9d)$$

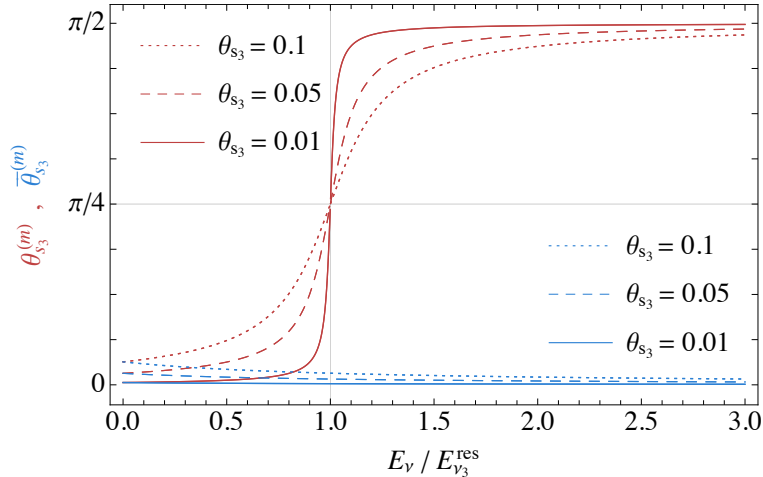


**Figure 2.** The in-medium effective mixing angles  $\theta_{S_3}^{(m)}$  (red curves) and  $\bar{\theta}_{S_3}^{(m)}$  (blue curves) between  $\nu_3 - S_3$  and  $\bar{\nu}_3 - \bar{S}_3$ , respectively. The dependence of these angles is shown as a function of (anti)neutrino energy  $E_\nu$  in units of the resonant energy  $E_{\nu_3}^{\text{res}}$  for different choices of the vacuum mixing angle  $\theta_{S_3}$ .

where  $C_3$  and the effective  $\nu_3 - S_3$  mixing angle in matter,  $\theta_{S_3}^{(m)}$ , are defined through:

$$\sin 2\theta_{S_3}^{(m)} = \frac{\sin 2\theta_{S_3}}{C_3} \equiv \frac{\sin 2\theta_{S_3}}{\sqrt{(\sin 2\theta_{S_3})^2 + \left(\cos 2\theta_{S_3} - \frac{4E_\nu}{\delta M_3^2} \frac{|\Delta V|}{2}\right)^2}}. \quad (2.10)$$

Expressions analogous to (2.9a)–(2.9d) and (2.10) hold for antineutrinos, with one important difference:  $-|\Delta V|$  should be replaced everywhere by  $+|\Delta V|$ . Note, importantly, that because of our choice of sign for the matter potential  $\Delta V$ ,  $\nu_3 - S_3$  oscillations become *resonant* (*i.e.*, the mixing angle becomes maximal,  $\theta_{S_3}^{(m)} = \pi/4$ ) when  $E_\nu$  is at the resonant energy value of

$$E_{\nu_3}^{\text{res}} = \frac{\delta M_3^2 \cos 2\theta_{S_3}}{2|\Delta V|}. \quad (2.11)$$

Because the matter potential for antineutrinos has the opposite sign, no such resonant effect is present for  $\bar{\nu}_3 - \bar{S}_3$  oscillations.

Fig. 2 displays the effective active-sterile mixing angles in matter for both neutrinos ( $\theta_{S_3}^{(m)}$ ) and antineutrinos ( $\bar{\theta}_{S_3}^{(m)}$ ) as a function of (anti-)neutrino energy, under three illustrative assumptions for the vacuum mixing angle  $\theta_{S_3}$ . Note that the transition from  $\theta_{S_3}^{(m)} \approx \theta_{S_3}$  to  $\theta_{S_3}^{(m)} \rightarrow \pi/2$  as  $E_\nu$  crosses the resonant region becomes sharper for smaller values of the vacuum mixing angle  $\theta_{S_3}$ . For antineutrinos, on the other hand, the active-sterile mixing angle  $\bar{\theta}_{S_3}^{(m)}$  decreases monotonically with increasing energy (see also Subsec. 2.3).

## 2.1 Neutrino propagation eigenstates in three energy regimes

With (2.9a)–(2.9d) and (2.10), we can now proceed to discuss the composition of the propagation eigenstates at finite matter density, and their respective oscillation phases, in three energy regimes relative to the resonant energy  $E_{\nu_3}^{\text{res}}$  defined in (2.11).

- **At very low energies**,  $E_\nu \ll E_{\nu_3}^{\text{res}}$ , or alternatively, at very low medium densities,  $|\Delta V| \rightarrow 0$ , we recover the vacuum oscillation results, with the mixing angle between  $\nu_3$  and  $S_3$  being

$$\theta_{S_3}^{(m)} \simeq \theta_{S_3} \quad (2.12)$$

and the propagation eigenstates and respective oscillation phases given by:

$$|N_{1,m}\rangle = |\nu_1\rangle, \quad \omega_1 = \frac{\delta m_{13}^2}{2E_\nu} \quad (2.13a)$$

$$|N_{2,m}\rangle = |\nu_2\rangle, \quad \omega_2 = \frac{\delta m_{23}^2}{2E_\nu} \quad (2.13b)$$

$$|N_{3,m}^{(-)}\rangle = -\sin\theta_{S_3} |S_3\rangle + \cos\theta_{S_3} |\nu_3\rangle, \quad \omega_3^{(-)} \simeq -\frac{\sin^2\theta_{S_3} \delta M_3^2}{2E_\nu} \left( \frac{E_\nu}{E_{\nu_3}^{\text{res}}} \cos 2\theta_{S_3} \right) \quad (2.13c)$$

$$|N_{3,m}^{(+)}\rangle = \cos\theta_{S_3} |S_3\rangle + \sin\theta_{S_3} |\nu_3\rangle, \quad \omega_3^{(+)} \simeq \frac{\delta M_3^2}{2E_\nu} \left( 1 - \frac{E_\nu}{E_{\nu_3}^{\text{res}}} \cos 2\theta_{S_3} \right) \quad (2.13d)$$

- **At the resonance**,  $E_\nu = E_{\nu_3}^{\text{res}}$ , the mixing between  $\nu_3$  and  $S_3$  is maximal,

$$\theta_{S_3}^{(m)} = \frac{\pi}{4}, \quad (2.14)$$

and the propagation eigenstates and respective oscillation phases are given by:

$$|N_{1,m}\rangle = |\nu_1\rangle, \quad \omega_1 = \frac{\delta m_{13}^2}{2E_\nu} \quad (2.15a)$$

$$|N_{2,m}\rangle = |\nu_2\rangle, \quad \omega_2 = \frac{\delta m_{23}^2}{2E_\nu} \quad (2.15b)$$

$$|N_{3,m}^{(-)}\rangle = \frac{1}{\sqrt{2}} (|\nu_3\rangle - |S_3\rangle), \quad \omega_3^{(-)} \simeq -\frac{\sin\theta_{S_3} \delta M_3^2}{2E_\nu} \quad (2.15c)$$

$$|N_{3,m}^{(+)}\rangle = \frac{1}{\sqrt{2}} (|\nu_3\rangle + |S_3\rangle), \quad \omega_3^{(+)} \simeq +\frac{\sin\theta_{S_3} \delta M_3^2}{2E_\nu} \quad (2.15d)$$

- **At very high energies**,  $E_\nu \gg E_{\nu_3}^{\text{res}}$ , the mixing between  $\nu_3$  and  $S_3$  is strongly suppressed, with

$$\theta_{S_3}^{(m)} \rightarrow \frac{\pi}{2}, \quad (2.16)$$

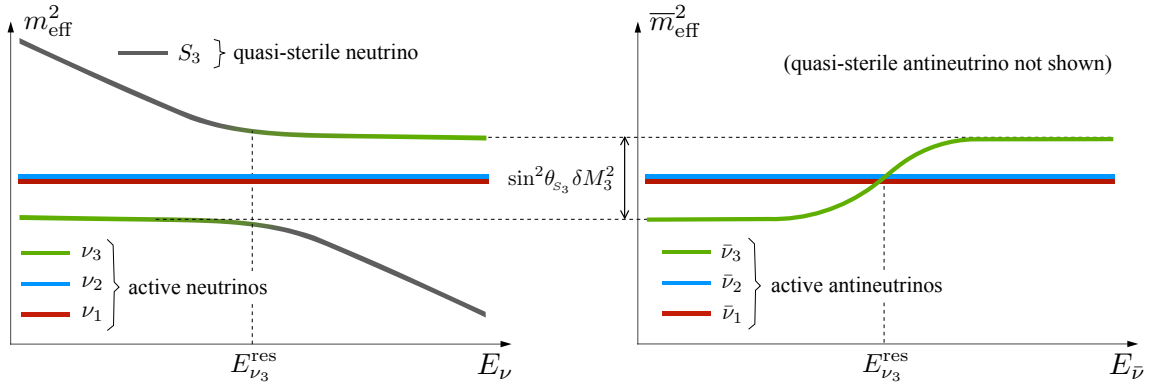


**Figure 3.** [For illustration purposes only—not to scale] Effective mass-squared eigenvalues of neutrino propagation eigenstates (left panel) and antineutrino propagation eigenstates (right panel) as a function of (anti-)neutrino energy in the quasi-sterile neutrino toy model. The eigenstates’ flavor compositions are denoted by their color shading.

so that their hierarchy is inverted, the active neutrino  $\nu_3$  becomes the heavier eigenstate, and the sterile neutrino  $S_3$  becomes the lighter eigenstate:

$$|N_{1,m}\rangle = |\nu_1\rangle, \quad \omega_1 = \frac{\delta m_{13}^2}{2E_\nu} \quad (2.17a)$$

$$|N_{2,m}\rangle = |\nu_2\rangle, \quad \omega_2 = \frac{\delta m_{23}^2}{2E_\nu} \quad (2.17b)$$

$$|N_{3,m}^{(-)}\rangle \rightarrow -|S_3\rangle, \quad \omega_3^{(-)} \simeq \frac{\delta M_3^2}{2E_\nu} \left(1 - \frac{E_\nu}{E_{\nu_3}^{\text{res}}} \cos 2\theta_{S_3}\right) \quad (2.17c)$$

$$|N_{3,m}^{(+)}\rangle \rightarrow |\nu_3\rangle, \quad \omega_3^{(+)} \simeq \frac{\sin^2\theta_{S_3} \delta M_3^2}{2E_\nu} \left(1 + \frac{E_{\nu_3}^{\text{res}}}{E_\nu}\right) \quad (2.17d)$$

Importantly, at high very neutrino energies  $E_\nu \rightarrow \infty$ , the active neutrino  $\nu_3$  receives an effective contribution to its mass of  $\delta m_3^2 = \sin^2\theta_{S_3} \delta M_3^2$  (note (2.17d)), an effect that has been previously noted in [57–60]. Compatibility with observations from high energy atmospheric and accelerator neutrinos then enforces only two possibilities:

- a) The effective mass contribution to  $\nu_3$  should be extremely suppressed so as to not make any difference, *i.e.*, it should be of order of the current experimental uncertainty on the atmospheric mass-squared splitting. Quantitatively, this would imply

$$\sin^2\theta_{S_3} \delta M_3^2 \lesssim \mathcal{O}(10^{-4}) \text{ eV}^2. \quad (2.18)$$

- b) In vacuum, the active neutrino mass hierarchy is inverted, and at high neutrino energies  $E_\nu \gg E_{\nu_3}^{\text{res}}$  the effective mass contribution to  $\nu_3$  due to matter effects

flips the neutrino mass ordering to a normal hierarchy. This would require

$$\begin{aligned}\sin^2\theta_{S_3} \delta M_3^2 &\simeq 2 |\delta m_{32}^2| \\ &\sim (5 \pm 0.5) \times 10^{-3} \text{ eV}^2.\end{aligned}\tag{2.19}$$

Option (a) above would preclude any detectable effect at MiniBooNE, and therefore, while perfectly compatible with experimental constraints, it is not relevant for this minimal model case study. Which leaves us with (b) as the only option of interest.

Figs. 2 and 3 provide a clear illustration of three energy regimes discussed, as well as the transitions between them. In particular, Fig. 3 (left panel) depicts how the composition and eigenvalues of the propagation eigenstates change as the neutrino energy crosses the resonant region set by  $E_{\nu_3}^{\text{res}}$ .

## 2.2 Neutrino oscillation probabilities

We can now proceed to derive various appearance and disappearance oscillation probabilities. The first step is to obtain the flavor eigenstates as a function of the propagation eigenstates in (2.9).

Inverting the relations in (2.9c) and (2.9d), we have:

$$|\nu_3\rangle = \cos\theta_{S_3}^{(m)} |N_{3,m}^{(-)}\rangle + \sin\theta_{S_3}^{(m)} |N_{3,m}^{(+)}\rangle\tag{2.20a}$$

$$|S_3\rangle = -\sin\theta_{S_3}^{(m)} |N_{3,m}^{(-)}\rangle + \cos\theta_{S_3}^{(m)} |N_{3,m}^{(+)}\rangle\tag{2.20b}$$

Using (2.3) and (2.20a), the muon-neutrino flavor is then given by:

$$\begin{aligned}|\nu_\mu\rangle &= U_{\mu 1}^* |\nu_1\rangle + U_{\mu 2}^* |\nu_2\rangle + U_{\mu 3}^* |\nu_3\rangle \\ &= U_{\mu 1}^* |\nu_1\rangle + U_{\mu 2}^* |\nu_2\rangle + U_{\mu 3}^* \cos\theta_{S_3}^{(m)} |N_{3,m}^{(-)}\rangle + U_{\mu 3}^* \sin\theta_{S_3}^{(m)} |N_{3,m}^{(+)}\rangle,\end{aligned}\tag{2.21}$$

which, after propagating through a distance  $L$ , is time-evolved to:

$$\begin{aligned}|\nu_\mu(L)\rangle &= U_{\mu 1}^* e^{-i\omega_1 L} |\nu_1\rangle + U_{\mu 2}^* e^{-i\omega_2 L} |\nu_2\rangle \\ &\quad + U_{\mu 3}^* \cos\theta_{S_3}^{(m)} e^{-i\omega_3^{(-)} L} |N_{3,m}^{(-)}\rangle + U_{\mu 3}^* \sin\theta_{S_3}^{(m)} e^{-i\omega_3^{(+)} L} |N_{3,m}^{(+)}\rangle.\end{aligned}\tag{2.22}$$

Likewise, the electron-neutrino flavor is given by:

$$\begin{aligned}|\nu_e\rangle &= U_{e 1}^* |\nu_1\rangle + U_{e 2}^* |\nu_2\rangle + U_{e 3}^* |\nu_3\rangle \\ &= U_{e 1}^* |\nu_1\rangle + U_{e 2}^* |\nu_2\rangle + U_{e 3}^* \cos\theta_{S_3}^{(m)} |N_{3,m}^{(-)}\rangle + U_{e 3}^* \sin\theta_{S_3}^{(m)} |N_{3,m}^{(+)}\rangle,\end{aligned}\tag{2.23}$$

and through propagation evolves to:

$$\begin{aligned}|\nu_e(L)\rangle &= U_{e 1}^* e^{-i\omega_1 L} |\nu_1\rangle + U_{e 2}^* e^{-i\omega_2 L} |\nu_2\rangle \\ &\quad + U_{e 3}^* \cos\theta_{S_3}^{(m)} e^{-i\omega_3^{(-)} L} |N_{3,m}^{(-)}\rangle + U_{e 3}^* \sin\theta_{S_3}^{(m)} e^{-i\omega_3^{(+)} L} |N_{3,m}^{(+)}\rangle.\end{aligned}\tag{2.24}$$

We note that the expressions (2.22) and (2.24) above are valid for neutrino propagation through a medium with constant density and composition. In cases where the medium density/composition changes as the neutrino propagates, so does the Hamiltonian change. In such cases, (2.22) and (2.24) have to be replaced with the appropriate states propagated under time-ordered Hamiltonian evolution.

The  $\nu_\mu \rightarrow S_3$  oscillation probability is then given by:

$$\begin{aligned} P(\nu_\mu \rightarrow S_3) &\equiv |\langle S_3 | \nu_\mu(L) \rangle|^2 \\ &= |U_{\mu 3}|^2 \sin^2 2\theta_{S_3}^{(m)} \sin^2 \left( \frac{C_3 \delta M_3^2}{4E_\nu} L \right), \end{aligned} \quad (2.25)$$

and the  $\nu_e \rightarrow S_3$  oscillation probability by:

$$\begin{aligned} P(\nu_e \rightarrow S_3) &\equiv |\langle S_3 | \nu_e(L) \rangle|^2 \\ &= |U_{e 3}|^2 \sin^2 2\theta_{S_3}^{(m)} \sin^2 \left( \frac{C_3 \delta M_3^2}{4E_\nu} L \right). \end{aligned} \quad (2.26)$$

Finally, the  $\nu_\mu \rightarrow \nu_e$  appearance probability is given by:

$$\begin{aligned} P(\nu_\mu \rightarrow \nu_e) &= |\langle \nu_e | \nu_\mu(L) \rangle|^2 \\ &= \left| U_{e1} U_{\mu 1}^* e^{-i\omega_1 L} + U_{e2} U_{\mu 2}^* e^{-i\omega_2 L} \right. \\ &\quad \left. + U_{e3} U_{\mu 3}^* \cos^2 \theta_{S_3}^{(m)} e^{-i\omega_3^{(-)} L} + U_{e3} U_{\mu 3}^* \sin^2 \theta_{S_3}^{(m)} e^{-i\omega_3^{(+)} L} \right|^2. \end{aligned} \quad (2.27)$$

In MiniBooNE, the baseline-to-energy ratio is in the range of  $L/E_\nu \sim \mathcal{O}(1-10)$  eV<sup>-2</sup>. Therefore, when computing the  $\nu_e$  appearance probabilities at MiniBooNE, we can ignore the difference in oscillation phases between the two ‘solar’ neutrino states  $\nu_1$  and  $\nu_2$ , since  $(\omega_2 L - \omega_1 L)|_{\text{MB}} \sim \mathcal{O}(10^{-5} - 10^{-4})$ . In this case we have

$$P(\nu_\mu \rightarrow \nu_e) \Big|_{\text{MB}} \simeq |U_{e3}|^2 |U_{\mu 3}|^2 \left| -e^{-i\omega_2 L} + \cos^2 \theta_{S_3}^{(m)} e^{-i\omega_3^{(-)} L} + \sin^2 \theta_{S_3}^{(m)} e^{-i\omega_3^{(+)} L} \right|^2. \quad (2.28)$$

We can look at three energy regimes of MiniBooNE’s appearance probability in (2.28):

**For low energy neutrinos**,  $E_\nu \ll E_{\nu_3}^{\text{res}}$ , or alternatively, at negligible medium densities,  $V_m \rightarrow 0$ , the appearance probability (2.28) reduces to the familiar form:

$$P(\nu_\mu \rightarrow \nu_e) \Big|_{E_\nu \rightarrow 0} \approx 4 |U_{e3}|^2 |U_{\mu 3}|^2 \sin^4 \theta_{S_3} \sin^2 \left( \frac{\delta M_3^2}{4E_\nu} L \right). \quad (2.29)$$

**At the resonance**,  $E_\nu = E_{\nu_3}^{\text{res}}$ ,

$$P(\nu_\mu \rightarrow \nu_e) \Big|_{E_{\nu_3}^{\text{res}}} \approx 4 |U_{e3}|^2 |U_{\mu 3}|^2 \left[ \sin^2 \left( \frac{2 \delta m_{32}^2 / \sin \theta_{S_3}}{4 E_{\nu_3}^{\text{res}}} L \right) - \frac{1}{4} \sin^2 \left( \frac{4 \delta m_{32}^2 / \sin \theta_{S_3}}{4 E_{\nu_3}^{\text{res}}} L \right) \right], \quad (2.30)$$

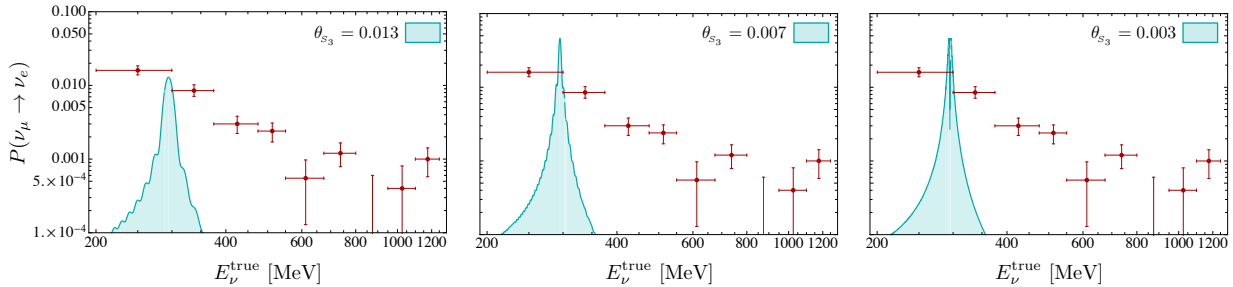


**Figure 4.** The  $\nu_\mu \rightarrow \nu_e$  appearance probability at MiniBooNE, as a function of true neutrino energy, predicted by the toy model (2.28) assuming  $E_{\nu_3}^{\text{res}}|_{\text{MB}} = 295$  MeV. Three different choices for the active-sterile vacuum mixing angle  $\theta_{s_3}$  are shown: below (left panel), at (middle panel), and above (right panel) the appearance probability saturation condition; see (2.31) and (2.32). The red data points with error bars were taken from Fig. 21 of [22]; they assume  $E_\nu^{\text{true}} \sim E_\nu^{\text{QE}}$ , which is a very coarse approximation. As such, they should be interpreted as a *qualitative* measure of MiniBooNE’s anomalous appearance probabilities.

where we have used (2.19). Note that the  $\nu_e$  appearance probability is maximized at the resonance, and, in the case of (2.30), it is upper-bounded by  $4|U_{e3}|^2|U_{\mu 3}|^2 \sim (0.04 - 0.06)$ . It peaks at:

$$\frac{\delta m_{32}^2}{\sin \theta_{s_3}} \frac{L}{E_{\nu_3}^{\text{res}}} = (2n + 1)\pi, \quad n \in \mathbb{Z}. \quad (2.31)$$

If we set  $L$  in (2.31) to MiniBooNE’s baseline<sup>2</sup> of  $L|_{\text{MB}} = 490$  m, and also set  $n = 0$  or  $n = -1$ , we can obtain the maximum value of  $|\sin \theta_{s_3}|$  that is able to saturate the appearance probability at the resonance. Choosing  $E_{\nu_3}^{\text{res}}|_{\text{MB}} = 300$  MeV for concreteness, we have

$$|\sin \theta_{s_3}^{(\text{max})}| = \left. \frac{|\delta m_{32}^2|}{\pi} \frac{L}{E_{\nu_3}^{\text{res}}} \right|_{\text{MB}} \Rightarrow |\theta_{s_3}^{(\text{max})}| \simeq 6.6 \times 10^{-3}. \quad (2.32)$$

Fig. 4 shows the toy model’s  $\nu_e$  appearance probability at MiniBooNE for  $E_{\nu_3}^{\text{res}}|_{\text{MB}} = 295$  MeV and three different choices of  $|\theta_{s_3}|$ . In the left panel  $|\theta_{s_3}| > |\theta_{s_3}^{(\text{max})}|$ , and therefore the  $\nu_e$  appearance probability is below the saturation condition in (2.31). In the middle panel  $|\theta_{s_3}| \approx |\theta_{s_3}^{(\text{max})}|$ ; the appearance probability is saturated and displays a single sharp peak at the resonant energy. Finally, in the right panel  $|\theta_{s_3}| < |\theta_{s_3}^{(\text{max})}|$ ; the appearance probability is saturated but oscillates rapidly within the resonant region.

The span of the resonant region is nearly-independent of  $\theta_{s_3}$  and  $E_{\nu_3}^{\text{res}}|_{\text{MB}}$ . As a rough approximation, we can consider the width of the resonant oscillations’ envelope,  $\Delta E^{\text{res}}$ ,

<sup>2</sup>The center of the MiniBooNE detector is located 541 m from the production target; however, the baseline’s first  $\sim 50$  m constitute the decay region [77]. Hence, the beam neutrinos propagate in matter through a distance of  $\sim 490$  m. In this specific case, the evolution of the initial  $\nu_\mu$  state through the decay region can be neglected, and the MiniBooNE baseline can be set to  $L|_{\text{MB}} = 490$  m.

whose magnitude is given by:

$$\begin{aligned}
\Delta E^{\text{res}}|_{\text{MB}} &\sim 2 |\tan 2\theta_{S_3}^{\text{(max)}}| E_{\nu_3}^{\text{res}}|_{\text{MB}} \\
&\sim \frac{4}{\pi} |\delta m_{32}^2| L|_{\text{MB}} \\
&\sim 8 \text{ MeV},
\end{aligned} \tag{2.33}$$

which is narrow for MiniBooNE’s detector resolution. Averaging the oscillation probability within the resonant range  $\Delta E^{\text{res}}$  yields about (40 – 45)% of the peak value of  $4|U_{e3}|^2|U_{\mu 3}|^2$ ; *i.e.*,  $P(\nu_\mu \rightarrow \nu_e) \sim (1.6 - 2.7)\%$  in the resonant region. Nuclear effects and energy resolution preclude the MiniBooNE detector from resolving such a narrow peak in the energy distribution of  $\nu_e$  events. Smearing this rate over the average bin size of 100 MeV, we obtain an average appearance probability of roughly (0.3 – 0.5)% within the 200 – 300 MeV range, which is still too small to account for the reported excess in appearance probability of 1.4 – 1.8% in this energy bin [22]. This is compounded by the fact that this model predicts a negligible  $\nu_e$  appearance probability in the regions outside the resonant region, including MiniBooNE’s higher energy bins with reported excesses (see Fig. 4). This constitutes one of three important reasons why this minimal model falls short of explaining the MiniBooNE excess. We will come back to this issue shortly.

**For very high energy neutrinos**,  $E_\nu \gg E_{\nu_3}^{\text{res}}$ , or alternatively, in very dense matter,  $|\Delta V| \gg \delta M_3^2/E_\nu$ , (2.28) reduces to:

$$P(\nu_\mu \rightarrow \nu_e) \Big|_{E_\nu \gg E_{\nu_3}^{\text{res}}} \approx 4|U_{e3}|^2|U_{\mu 3}|^2 \sin^2 \left[ \frac{\delta m_{32}^2 (1 + 2 E_{\nu_3}^{\text{res}}/E_\nu)}{4E_\nu} L \right]. \tag{2.34}$$

Note that (2.34) recovers the SM limit of  $\nu_\mu \rightarrow \nu_e$  oscillation probabilities at very high energies, since the effective mass-squared splitting controlling these oscillations, namely,  $\delta m_{32}^2 (1 + 2 E_{\nu_3}^{\text{res}}/E_\nu)$ , approaches the SM value of  $\delta m_{32}^2$  as  $E_{\nu_3}^{\text{res}}/E_\nu \rightarrow 0$ . (As discussed in option (b) of Subsec. 2.1, this is because the condition in (2.19) effectively flips the active neutrino in-medium mass hierarchy at high energies.)

Unfortunately, however, the active neutrino mass ordering does not relax to the SM expectation quickly enough at high energies, leading to strong tensions with measurements from long-baseline neutrino experiments. Consider, for instance, T2K’s measurement of  $\delta m_{32}^2$  in neutrino mode. T2K’s baseline is  $L|_{\text{T2K}} = 295 \text{ km}$ , and its resonant energy is related to that of MiniBooNE’s by:

$$\begin{aligned}
E_{\nu_3}^{\text{res}}|_{\text{T2K}} &\approx E_{\nu_3}^{\text{res}}|_{\text{MB}} \frac{\rho|_{\text{MB}}}{\rho|_{\text{T2K}}} \\
&\sim E_{\nu_3}^{\text{res}}|_{\text{MB}} \frac{1.2 \text{ g/cm}^3}{2.8 \text{ g/cm}^3},
\end{aligned} \tag{2.35}$$

which, for the benchmark choice of  $E_{\nu_3}^{\text{res}}|_{\text{MB}} = 300 \text{ MeV}$ , gives  $E_{\nu_3}^{\text{res}}|_{\text{T2K}} \sim 129 \text{ MeV}$ . Further, T2K’s determination of  $\delta m_{32}^2$  is dominated by its sensitivity to the dip in the  $\nu_\mu$  survival

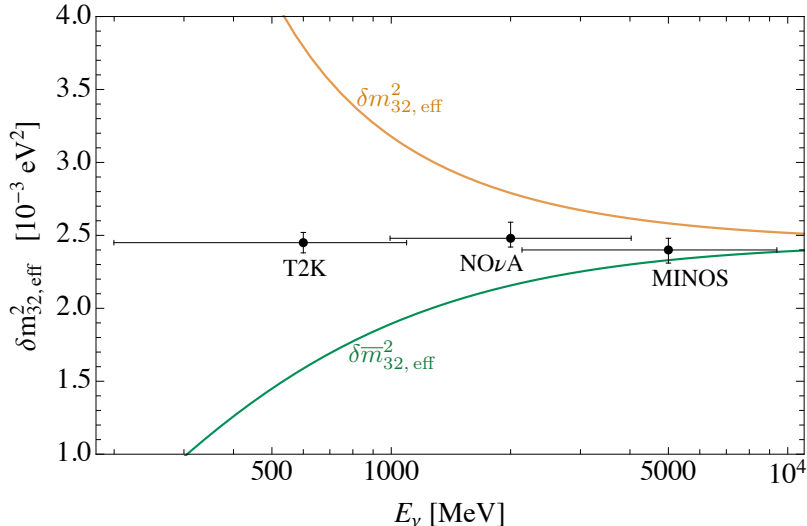


**Figure 5.** The effective ‘atmospheric’ mass-squared splitting predicted by the toy model for both neutrinos ( $\delta m_{32, \text{eff}}^2$ ) and antineutrinos ( $\delta \bar{m}_{32, \text{eff}}^2$ ) as a function of (anti-)neutrino energy, assuming  $\theta_{s_3} = 0.003$  and  $E_{\nu_3}^{\text{res}}|_{\text{MB}} \sim 300$  MeV. The data points with error bars denote recent measurements of  $\delta m_{32}^2$  by long-baseline accelerator experiments [79–81].

probability at around  $E_{\nu_\mu}^{\text{dip}}|_{\text{T2K}} \sim 600$  MeV. Using (2.34), the effective  $\delta m_{32, \text{eff}}^2$  predicted at T2K in this energy range would be:

$$\begin{aligned} \delta m_{32, \text{eff}}^2|_{\text{T2K}} &\sim |\delta m_{32}^2|_{\text{SM}} \times \left(1 + 2 \frac{E_{\nu_3}^{\text{res}}}{E_{\nu_\mu}^{\text{dip}}}\right)\Bigg|_{\text{T2K}} \\ &\sim 1.43 \times |\delta m_{32}^2|_{\text{SM}}, \end{aligned} \quad (2.36)$$

which is in significant tension with neutrino data from T2K [78], whose error on its most recent determination of  $\delta m_{32}^2$  is only about 4%. This constitutes the second of three main reasons why this minimal model is phenomenologically unviable.

Fig. 5 shows this toy model’s prediction for the effective  $\delta m_{32, \text{eff}}^2$  as a function of neutrino energy in long-baseline neutrino experiments such as T2K [79], MINOS [80], and NO $\nu$ A [81]. Here, we take  $\theta_{s_3} = 0.003$  and make the same simplified assumption as in (2.35) that average matter density through which neutrinos propagate in these long-baseline experiments results in a long-baseline resonant energy of  $E_{\nu_3}^{\text{res}}|_{\text{T2K}} \sim 129$  MeV. It is clear from Fig. 5 that severe tensions between data and the toy model prediction for  $\delta m_{32, \text{eff}}^2$  persist even at much higher neutrino energies than the range probed by T2K.

### 2.3 Matter effects on antineutrinos

We now briefly discuss the consequences of the minimal model for antineutrinos. The sign of the matter potential,  $\Delta V$ , was chosen such that antineutrinos do not experience resonant oscillations. Furthermore, the maximum allowed strength of the  $\bar{\nu}_3 - \bar{S}_3$  mixing angle, given in (2.32), is too small to yield a significant amplitude for non-resonant  $\bar{\nu}_3 - \bar{S}_3$

oscillations (see also Fig. 2). Consequently, the  $\bar{\nu}_\mu \rightarrow \bar{\nu}_e$  appearance probability predicted by this minimal model is negligible, and therefore cannot account for the excesses of  $\bar{\nu}_e$ -like events reported by LSND and MiniBooNE. This is the third main reason why this minimal model is phenomenologically unviable.

Additionally, there is another shortcoming of the minimal model which is related to the second reason discussed at the end of Subsec. 2.2. Before we state it, we need to highlight how these BSM matter effects alter the in-medium oscillations of antineutrinos. Their propagation eigenstates are given by analogous expressions to (2.9) and (2.10) with  $|\Delta V| \rightarrow -|\Delta V|$ :

$$|\bar{N}_{1,m}\rangle = |\bar{\nu}_1\rangle, \quad \bar{\omega}_1 = \frac{\delta m_{13}^2}{2E_{\bar{\nu}}} \quad (2.37a)$$

$$|\bar{N}_{2,m}\rangle = |\bar{\nu}_2\rangle, \quad \bar{\omega}_2 = \frac{\delta m_{23}^2}{2E_{\bar{\nu}}} \quad (2.37b)$$

$$|\bar{N}_{3,m}^{(-)}\rangle = -\sin \bar{\theta}_{S_3}^{(m)} |\bar{S}_3\rangle + \cos \bar{\theta}_{S_3}^{(m)} |\bar{\nu}_3\rangle, \quad \bar{\omega}_3^{(-)} = \frac{\delta M_3^2}{4E_{\bar{\nu}}} \left(1 - \bar{C}_3 + \frac{E_{\bar{\nu}}}{E_{\nu_3}^{\text{res}}} \cos 2\theta_{S_3}\right) \quad (2.37c)$$

$$|\bar{N}_{3,m}^{(+)}\rangle = \cos \bar{\theta}_{S_3}^{(m)} |\bar{S}_3\rangle + \sin \bar{\theta}_{S_3}^{(m)} |\bar{\nu}_3\rangle, \quad \bar{\omega}_3^{(+)} = \frac{\delta M_3^2}{4E_{\bar{\nu}}} \left(1 + \bar{C}_3 + \frac{E_{\bar{\nu}}}{E_{\nu_3}^{\text{res}}} \cos 2\theta_{S_3}\right) \quad (2.37d)$$

where we have recast  $|\Delta V|$  in terms of  $E_{\nu_3}^{\text{res}}$  using (2.11). Furthermore,  $\bar{C}_3$  and the effective  $\bar{\nu}_3 - \bar{S}_3$  mixing angle in matter,  $\bar{\theta}_{S_3}^{(m)}$ , are defined through:

$$\sin 2\bar{\theta}_{S_3}^{(m)} = \frac{\sin 2\theta_{S_3}}{\bar{C}_3} \equiv \frac{\sin 2\theta_{S_3}}{\sqrt{(\sin 2\theta_{S_3})^2 + (\cos 2\theta_{S_3})^2 \left(1 + \frac{E_{\bar{\nu}}}{E_{\nu_3}^{\text{res}}}\right)^2}}. \quad (2.38)$$

Figs. 2 and 3 (right panel) illustrate, respectively, the in-medium  $\bar{\nu}_3 - \bar{S}_3$  mixing angle as a function of antineutrino energy, and the flavor composition and eigenvalues of the in-medium propagation eigenstates as a function of antineutrino energy.

We can proceed to examine two energy regimes of experimental interest: (i) the low energy region  $E_{\bar{\nu}} \sim \mathcal{O}(1 - 10)$  MeV, relevant for reactor experiments; and (ii) the high energy region  $E_{\bar{\nu}} \gtrsim (0.2 - 10)$  GeV, relevant for long-baseline accelerator experiments. Firstly, we note that in this minimal model  $\bar{\nu}_3 - \bar{S}_3$  mixing is always suppressed, and the active neutrino state  $\bar{\nu}_3$  is mostly composed of  $\bar{N}_3^{(-)}$ . Therefore, the effective antineutrino mass splitting  $\delta \bar{m}_{3i,\text{eff}}^2$  ( $i = 1, 2$ ) can be approximated by:

$$\begin{aligned} \delta \bar{m}_{3i,\text{eff}}^2 \Big|_{\bar{\nu}} &\simeq 2 E_{\bar{\nu}} (\bar{\omega}_3^{(-)} - \bar{\omega}_i) \\ &\rightarrow \begin{cases} -|\delta m_{3i}^2| \left(1 - 2 \cos 2\theta_{S_3} \frac{E_{\bar{\nu}}}{E_{\nu_3}^{\text{res}}}\right) & \text{for } E_{\bar{\nu}} \ll E_{\nu_3}^{\text{res}}, \\ |\delta m_{3i}^2| \left(1 - 2 \frac{E_{\nu_3}^{\text{res}}}{E_{\bar{\nu}}}\right) & \text{for } E_{\bar{\nu}} \gg E_{\nu_3}^{\text{res}}. \end{cases} \end{aligned} \quad (2.39)$$

Interestingly, as it is clear from (2.39), the antineutrino mass ordering in this minimal model displays the same ‘hierarchy-flipping’ pattern of the active neutrinos, with an inverted mass hierarchy in the asymptotically low energy limit and a normal in-medium mass hierarchy in the asymptotically high energy limit. This effect is illustrated in Fig. 3 (right panel).

Reactor-based antineutrino experiments such as Daya Bay [82] and RENO [83] have measured  $|\delta m_{31}^2|$  with  $\sim 5\%$  precision at  $2\sigma$  C.L. within the energy range  $E_{\bar{\nu}} \sim \mathcal{O}(1 - 10)$  MeV. From (2.39), we can check that the minimal model is within  $2\sigma$ -compatibility with these measurements, predicting

$$\delta \bar{m}_{31, \text{eff}}^2 \Big|_{\text{reactor } \bar{\nu}} \simeq - |\delta m_{31}^2|_{\text{SM}} \left[ 1 - 0.02 \times \left( \frac{E_{\bar{\nu}}}{3 \text{ MeV}} \right) \right]. \quad (2.40)$$

The minimal model’s compatibility with  $\bar{\nu}$ -data is not as good in the high energy limit, however. Several long-baseline accelerator experiments, such as K2K, T2K, MINOS, and NO $\nu$ A have also measured the active mass-squared splittings and mixing angles in antineutrino mode, albeit with less precision than in neutrino mode. Taking T2K again as an example, we can check the minimal model’s prediction for the effective  $\delta \bar{m}_{32, \text{eff}}^2$  that would be observed at T2K in antineutrino mode:

$$\begin{aligned} \delta \bar{m}_{32, \text{eff}}^2 \Big|_{\text{T2K}, \bar{\nu}} &\sim |\delta m_{32}^2|_{\text{SM}} \times \left( 1 - 2 \frac{E_{\nu_3}^{\text{res}}}{E_{\bar{\nu}\mu}^{\text{dip}}} \right) \Big|_{\text{T2K}} \\ &\sim 0.57 \times |\delta m_{32}^2|_{\text{SM}}, \end{aligned} \quad (2.41)$$

which is in significant tension with T2K’s most recent determination of  $\delta m_{32}^2$  in antineutrino mode [84], which had an error of  $\sim 8\%$ . This tension is analogous to the one (2.36) for neutrino mode, with the main difference being that the latter overpredicts  $|\delta m_{32}^2|$ , whereas the former underpredicts it. This is clearly illustrated in Fig. 5.

### 3 Beyond the minimal model: a viable explanation for the MiniBooNE excess

We begin this section by recapping the phenomenological shortcomings of the minimal model just discussed:

1. *The strength of the resonant  $\nu_\mu \rightarrow \nu_e$  oscillations in the minimal model is insufficient to account for the full low energy  $\nu_e$ -like excess at MiniBooNE.*

There are two reasons for this. First, the resonant energy window is very narrow. Second, the active neutrino experiencing resonant oscillations,  $\nu_3$ , has a suppressed  $\nu_e$  component, thereby suppressing the resonant amplitude by a factor of  $|U_{e3}|^2 |U_{\mu 3}|^2 \sim (0.01 - 0.015)$ , as shown in (2.28) and Fig. 4.

2. *The effective ‘atmospheric’ splitting  $\delta m_{32}^2$  predicted at long-baseline experiments is in strong tension with data.*

This is because, in the high energy regime  $E_\nu \gg E_{\nu_3}^{\text{res}}$ , the active state that mixes with the quasi-sterile state (which is  $\bar{\nu}_3$  in the minimal model) receives a residual

contribution to its in-medium effective mass given by (2.17d) for  $\nu_3$  and (2.37c) for  $\bar{\nu}_3$ . Hence, in order to preserve the expected active neutrino mass-squared splittings at high energies, the parameters of the minimal model have to be adjusted to effectively ‘flip’ the mass hierarchy at  $E_\nu \gg E_{\nu_3}^{\text{res}}$  according to (2.19). However, this hierarchy-flip does not happen ‘instantaneously’ as  $E_\nu$  crosses the resonant region—the effective mass-squared splitting  $\delta m_{32,\text{eff}}^2$  does not fully relax to the SM value until high enough energies, well above the energy range probed by, *e.g.*, T2K, NO $\nu$ A, and MINOS. As a result, the predicted  $\delta m_{32,\text{eff}}^2$  is in tension with accelerator-based measurements of  $\delta m_{32}^2$ , as shown in (2.36), (2.41), and Fig. 5.

3. *The minimal model cannot address the  $\bar{\nu}_e$ -like excesses at LSND and MiniBooNE, nor the  $\nu_e$ -like excess at MiniBooNE for ‘mid-energies’  $E_\nu \gtrsim 400$  MeV.*

This issue is related to 2 above. Since  $\nu_3 - S_3$  mixing has been constrained by the ‘hierarchy-flip’ relation in (2.19), this model predicts negligible appearance probabilities for  $\bar{\nu}_\nu \rightarrow \bar{\nu}_e$  oscillations, as well as for  $\nu_\nu \rightarrow \nu_e$  oscillations outside the resonant region (see Fig. 4).

The reasons behind these shortcomings, as summarized above, offer clues as to how the minimal model could be augmented and modified to overcome phenomenological tensions.

In particular, shortcoming 1 above could be addressed if  $\nu_1$  and/or  $\nu_2$ —which have larger  $\nu_e$  components—were involved in the resonant oscillation mechanism. However, this needs to be done in such a way that the effective mass spectrum of active neutrinos is not significantly altered at high energies. In other words, the incorporation of resonance effects for  $\nu_{1,2}$  in order to address shortcoming 1 must simultaneously address shortcoming 2.

The most straightforward way to achieve this goal is to augment the minimal model by introducing two additional quasi-sterile species,  $S_1$  and  $S_2$ , which will mix with  $\nu_1$  and  $\nu_2$ , respectively. This will result in two new resonant energies,  $E_{\nu_1}^{\text{res}}$  and  $E_{\nu_2}^{\text{res}}$ , which must fall within the low energy window of interest for MiniBooNE. These additional resonances will be weighted by factors of  $|U_{e1}|^2|U_{\mu 1}|^2$  and  $|U_{e2}|^2|U_{\mu 2}|^2$ , respectively, and therefore will allow for much larger resonant appearance probabilities than the minimal model. Furthermore, the parameters of this augmented model must be arranged such that the effective shift in the active neutrino masses is the same for  $\nu_1$ ,  $\nu_2$ , and  $\nu_3$ , so that the in-medium active mass hierarchy is preserved at high energies  $E_\nu \gg E_{\nu_{1,2,3}}^{\text{res}}$ . It turns out that this latter requirement will be sufficient to address shortcoming 2 as well, as we will detail shortly.

Unfortunately, the model’s augmentation by two new quasi-sterile states  $S_1$  and  $S_2$  is still insufficient to address shortcoming 3. As we shall see, this is because the three resonant regions will remain narrow, and  $\bar{\nu}_i - \bar{S}_i$  oscillations will remain suppressed away from the resonant region. Therefore, a fully viable model would still need an additional source of non-resonant active-to-sterile oscillations. The simplest option is to introduce a new ‘vanilla’ sterile neutrino that is neutral under the dark sector gauge interactions, and therefore does not experience a matter potential. This vanilla-sterile state will mix with a linear combination of active neutrinos to generate an off-resonance appearance probability, and, importantly, it will not qualitatively interfere with the resonant mechanism. This

ordinary ‘3+1’-like mechanism is well-known for providing an excellent fit to the LSND oscillation data, as well as to the MiniBooNE oscillation data for antineutrinos and mid-energy neutrinos. If one wishes, the vanilla ‘3+1’ parameters could also be adjusted to fit  $\bar{\nu}_e$  disappearance data, such as the Gallium and/or reactor anomalies, in the spirit of global fits.

Our goal in this study, however, is not to perform global fits of this model, much less re-fit the vanilla ‘3+1’ parameters to all existing neutrino data (something that has already been done *ad nauseam* in the literature; see, *e.g.*, [32, 85–91]). Instead, we will benchmark the vanilla ‘3+1’ parameters to yield a good fit to the LSND, MiniBooNE- $\bar{\nu}$ -mode, and Gallium anomalies, and focus our attention on deconstructing the parameter space of the resonant mechanism.

### 3.1 Full Model — Part I: the triple-resonance mechanism

For pedagogical purposes, we begin by describing the resonant mechanism of the full model with the ‘3+1’ non-resonant effects tuned off. In the next subsection, we will then introduce the ‘vanilla’-sterile state to complete the description of the full model.

As stated in the previous subsection, the full model will contain three quasi-sterile neutrinos,  $S_1$ ,  $S_2$ , and  $S_3$ , all of which experience the same effective matter potential in (2.7). Each of the  $S_i$  will mix exclusively with  $\nu_i$  with a vacuum mixing angle  $\theta_{S_i}$ , in a manner analogous to the  $\nu_3 - S_3$  mixing discussed in Sec. 2.

The effective matter Hamiltonian in the basis  $B = \{|\nu_1\rangle, |S_1\rangle, |\nu_2\rangle, |S_2\rangle, |\nu_3\rangle, |S_3\rangle\}$  can then be written in block-diagonal form as:

$$\hat{H}_{B, \text{matter}} = \begin{pmatrix} \hat{H}_1^{(2 \times 2)} & & \\ & \hat{H}_2^{(2 \times 2)} & \\ & & \hat{H}_3^{(2 \times 2)} \end{pmatrix} \quad (3.1)$$

where each block  $\hat{H}_i^{(2 \times 2)}$  acts on the subspace  $\{|\nu_i\rangle, |S_i\rangle\}$  and is defined by:

$$\begin{aligned} \hat{H}_i = \hat{H}[\nu_i, S_i] &\equiv \begin{pmatrix} \cos \theta_{S_i} & \sin \theta_{S_i} \\ -\sin \theta_{S_i} & \cos \theta_{S_i} \end{pmatrix} \cdot \begin{pmatrix} \frac{m_i^2}{2E_\nu} & 0 \\ 0 & \frac{M_i^2}{2E_\nu} \end{pmatrix} \cdot \begin{pmatrix} \cos \theta_{S_i} & -\sin \theta_{S_i} \\ \sin \theta_{S_i} & \cos \theta_{S_i} \end{pmatrix} - \begin{pmatrix} 0 & 0 \\ 0 & |\Delta V| \end{pmatrix} \\ &= \frac{m_i^2}{2E_\nu} \begin{pmatrix} 1 & 0 \\ 0 & 0 \end{pmatrix} + \frac{\delta M_i^2}{4E_\nu} \begin{pmatrix} 1 - \frac{E_\nu}{E_{\nu_i}^{\text{res}}} \cos 2\theta_{S_i} & \\ & \end{pmatrix} \begin{pmatrix} 1 & 0 \\ 0 & 1 \end{pmatrix} \\ &\quad + \frac{\delta M_i^2}{4E_\nu} \begin{pmatrix} -\cos 2\theta_{S_i} \left(1 - \frac{E_\nu}{E_{\nu_i}^{\text{res}}}\right) & \sin 2\theta_{S_i} \\ \sin 2\theta_{S_i} & \cos 2\theta_{S_i} \left(1 - \frac{E_\nu}{E_{\nu_i}^{\text{res}}}\right) \end{pmatrix}. \end{aligned} \quad (3.2)$$

Above,  $\delta M_i^2 \equiv M_i^2 - m_i^2$ , and  $M_i$  is the (vacuum) mass of the heavier eigenstate, which is composed predominantly of the sterile state  $S_i$ . Note that in the second line of (3.2) we have traded the matter potential  $|\Delta V|$  for  $E_{\nu_i}^{\text{res}}$  using:

$$|\Delta V| = \frac{\delta M_1^2}{2 E_{\nu_1}^{\text{res}}} \cos 2\theta_{S_1} = \frac{\delta M_2^2}{2 E_{\nu_2}^{\text{res}}} \cos 2\theta_{S_2} = \frac{\delta M_3^2}{2 E_{\nu_3}^{\text{res}}} \cos 2\theta_{S_3}. \quad (3.3)$$

In analogy with (2.9), we can proceed to diagonalize (3.2) to obtain the propagation eigenstates for  $i = 1, 2, 3$ :

$$|N_{i,m}^{(-)}\rangle = -\sin\theta_{S_i}^{(m)}|S_i\rangle + \cos\theta_{S_i}^{(m)}|\nu_i\rangle, \quad \omega_i^{(-)} = \frac{m_i^2}{2E_\nu} + \frac{\delta M_i^2}{4E_\nu} \left(1 - C_i - \frac{E_\nu}{E_{\nu_i}^{\text{res}}} \cos 2\theta_{S_i}\right) \quad (3.4a)$$

$$|N_{i,m}^{(+)}\rangle = \cos\theta_{S_i}^{(m)}|S_i\rangle + \sin\theta_{S_i}^{(m)}|\nu_i\rangle, \quad \omega_i^{(+)} = \frac{m_i^2}{2E_\nu} + \frac{\delta M_i^2}{4E_\nu} \left(1 + C_i - \frac{E_\nu}{E_{\nu_i}^{\text{res}}} \cos 2\theta_{S_i}\right) \quad (3.4b)$$

where, as usual,  $C_i$  and the effective  $\nu_i - S_i$  mixing angle in matter,  $\theta_{S_i}^{(m)}$ , are defined through:

$$\sin 2\theta_{S_i}^{(m)} = \frac{\sin 2\theta_{S_i}}{C_i} \equiv \frac{\sin 2\theta_{S_i}}{\sqrt{(\sin 2\theta_{S_i})^2 + (\cos 2\theta_{S_i})^2 \left(1 - \frac{E_\nu}{E_{\nu_i}^{\text{res}}}\right)^2}}. \quad (3.5)$$

### 3.1.1 Accelerator constraints on the triple-resonance mechanism

We begin by discussing how this triple-resonance mechanism addresses shortcoming 2 of the minimal model. In the high energy limit of  $E_\nu \gg E_{\nu_{1,2,3}}^{\text{res}}$ , each active neutrino  $\nu_i$  is composed predominantly of the propagation eigenstate  $N_{i,m}^{(+)}$  in (3.4b), with an effective mass-squared given by:

$$m_{i,\text{eff}}^2 = 2E_\nu \omega_i^{(+)} \simeq m_i^2 + \sin^2\theta_{S_i} \delta M_i^2 \left(1 + \frac{E_\nu^{\text{res}}}{E_\nu}\right) \quad (3.6)$$

From (3.6), we see that in the asymptotically high energy limit of  $E_{\nu_i}^{\text{res}}/E_\nu \rightarrow 0$ , the active mass hierarchy is preserved, *i.e.*,  $\delta m_{ij,\text{eff}}^2 \rightarrow \delta m_{ij}^2$  ( $i, j = 1, 2, 3$ ), if:

$$\sin^2\theta_{S_1} \delta M_1^2 \approx \sin^2\theta_{S_2} \delta M_2^2 \approx \sin^2\theta_{S_3} \delta M_3^2. \quad (3.7)$$

While (3.7) may appear like an extremely fine-tuned relation, note that if we write explicitly the  $\nu_i - S_i$  mixing terms in the Lagrangian,

$$\mathcal{L} \supset \sum_{i=1,2,3} \left[ m_i^{(\text{mix})} (\nu_i S_i + \nu_i^c S_i^c) + M_i S_i S_i^c \right] + \dots, \quad (3.8)$$

the mass-mixing term  $m_i^{(\text{mix})}$  is essentially  $m_i^{(\text{mix})} = \sin\theta_{S_i} M_i$ . Hence, when considering this model from a UV completion perspective, one could envision model-building the relations in (3.7) by invoking global symmetries, instead of enforcing (3.7) via *ad hoc* fine-tuning. These same global symmetries would also provide a natural mechanism for the alignment of  $S_i - \nu_i$  mixing with the SM neutrino mass basis.

We can also check the triple-resonance mechanism's prediction for  $\delta m_{32,\text{eff}}^2$  at T2K in neutrino mode. Following the discussion at the end of Subsec. 2.2, and using (3.6) and (3.7), we have:

$$\begin{aligned} \delta m_{32,\text{eff}}^2 \Big|_{\text{T2K}} &\sim \delta m_{32}^2 \Big|_{\text{SM}} \left[ 1 + \frac{\sin^2\theta_{S_i} \delta M_i^2}{\delta m_{32}^2 \Big|_{\text{SM}}} \left( \frac{E_{\nu_3}^{\text{res}} - E_{\nu_2}^{\text{res}}}{E_{\nu_\mu}^{\text{dip}}} \right) \Big|_{\text{T2K}} \right] \quad (3.9) \\ &\sim \delta m_{32}^2 \Big|_{\text{SM}} \times (1 \pm 0.08) \quad (\text{from T2K's } \nu \text{ data}), \end{aligned}$$

where the second line in (3.9) is a  $2\sigma$ -constraint on this prediction to be compatible with T2K's determination of  $\delta m_{32}^2$  in neutrino mode [78]. Defining

$$R_{m_\nu^2} \equiv \frac{\sin^2 \theta_{S_i} \delta M_i^2}{|\delta m_{32}^2|_{\text{SM}}}, \quad (3.10)$$

remembering that  $E_{\nu_\mu}^{\text{dip}}|_{\text{T2K}} \sim 600$  MeV, and assuming the relation between  $E_{\nu_i}^{\text{res}}|_{\text{T2K}}$  and  $E_{\nu_i}^{\text{res}}|_{\text{MB}}$  in (2.35), we can recast the constraint in (3.9) as:

$$R_{m_\nu^2} \left[ \frac{|E_{\nu_3}^{\text{res}} - E_{\nu_2}^{\text{res}}|_{\text{MB}}}{\text{MeV}} \right] \lesssim 1.1 \times 10^2. \quad (3.11)$$

An analogous calculation for antineutrinos yields

$$\begin{aligned} \delta \bar{m}_{32, \text{eff}}^2|_{\text{T2K}, \bar{\nu}} &\sim \delta m_{32}^2|_{\text{SM}} \left[ 1 - \frac{\sin^2 \theta_{S_i} \delta M_i^2}{\delta m_{32}^2|_{\text{SM}}} \left( \frac{E_{\nu_3}^{\text{res}} - E_{\nu_2}^{\text{res}}}{E_{\bar{\nu}_\mu}^{\text{dip}}} \right) \Big|_{\text{T2K}} \right] \\ &\sim \delta m_{32}^2|_{\text{SM}} \times (1 \pm 0.16) \quad (\text{from T2K's } \bar{\nu} \text{ data}), \end{aligned} \quad (3.12)$$

which provides a weaker constraint than in (3.9, 3.11) because T2K's determination of  $\delta m_{32}^2$  in antineutrino mode is less precise [84].

### 3.1.2 Reactor constraints on the triple-resonance mechanism

Independent constraints on the parameters of the triple-resonance mechanism come from lower energy electron antineutrinos at short- and long-baselines reactor-based experiments.

We will not rehash the derivation of the antineutrino propagation eigenstates, which can be easily obtained by reversing the signs of  $|\Delta V|$  and  $E_\nu/E_{\nu_i}^{\text{res}}$  in (3.2), (3.4), and (3.5). In the low energy limit of  $E_{\bar{\nu}} \ll E_{\nu_{1,2,3}}^{\text{res}}$ , each active antineutrino  $\bar{\nu}_i$  is composed predominantly of the propagation eigenstate  $\bar{N}_{i,m}^{(-)}$ , with an effective mass-squared given by:

$$\bar{m}_{i, \text{eff}}^2|_{\bar{\nu}} = 2 E_{\bar{\nu}} \bar{\omega}_i^{(-)} \simeq m_i^2 + \sin^2 \theta_{S_i} \delta M_i^2 \left( \frac{E_{\bar{\nu}}}{E_{\nu_i}^{\text{res}}} \cos 2\theta_{S_i} \right). \quad (3.13)$$

With (3.13), we can revisit the prediction for  $\delta m_{31}^2$  from short-baseline reactor measurements (by, *e.g.*, Daya Bay and RENO), discussed at the end of Subsec. 2.3. Using Daya Bay for concreteness, we have,

$$\begin{aligned} \delta \bar{m}_{31, \text{eff}}^2|_{\text{reactor } \bar{\nu}_e} &\simeq \delta m_{31}^2|_{\text{SM}} \left[ 1 + R_{m_\nu^2} \frac{|\delta m_{32}^2|}{\delta m_{31}^2|_{\text{SM}}} \left( \frac{E_{\bar{\nu}_e}^{\text{dip}}}{E_{\nu_3}^{\text{res}}} - \frac{E_{\bar{\nu}_e}^{\text{dip}}}{E_{\nu_1}^{\text{res}}} \right) \Big|_{\text{DayaB}} \right] \\ &\sim \delta m_{31}^2|_{\text{SM}} \times (1 \pm 0.05) \quad (\text{from Daya Bay's } \bar{\nu}_e \text{ data at } 2\sigma). \end{aligned} \quad (3.14)$$

Above, we made the approximation  $\cos 2\theta_{S_i} \approx 1$  and used (3.10). Using  $E_{\bar{\nu}_e}^{\text{dip}}|_{\text{DayaB}} \sim 3$  MeV, we can recast the constraint in the second line of (3.14) as:

$$R_{m_\nu^2} \left[ \frac{|E_{\nu_3}^{\text{res}} - E_{\nu_1}^{\text{res}}|_{\text{MB}}}{\text{MeV}} \right] \lesssim 1.5 \times 10^3, \quad (3.15)$$

which is about an order-of-magnitude weaker than (3.11).

As for reactor  $\bar{\nu}_e$ 's at long-baselines, of interest to us is KamLAND's determination of the 'solar' mass-squared splitting  $\delta m_{21}^2$  with an error of  $\sim 2.5\%$  [92]. Using (3.13), we can obtain the triple-resonance mechanism's prediction for  $\delta \bar{m}_{21, \text{eff}}^2$  at KamLAND:

$$\begin{aligned} \delta \bar{m}_{21, \text{eff}}^2 \Big|_{\text{KamLAND}} &\simeq \delta m_{21}^2 \Big|_{\text{SM}} \left[ 1 + R_{m_\nu^2} \frac{|\delta m_{32}^2|}{\delta m_{21}^2} \Big|_{\text{SM}} \left( \frac{E_{\bar{\nu}_e}}{E_{\nu_2}^{\text{res}}} - \frac{E_{\bar{\nu}_e}}{E_{\nu_1}^{\text{res}}} \right) \Big|_{\text{KamL}} \right] \quad (3.16) \\ &\sim \delta m_{21}^2 \Big|_{\text{SM}} \times (1 \pm 0.05) \quad (\text{from KamLAND's } \bar{\nu}_e \text{ data at } 2\sigma). \end{aligned}$$

KamLAND observes  $\bar{\nu}_e$ 's with energies ranging from  $E_{\bar{\nu}_e} \sim (0.9 - 7)$  MeV. As a simplification, we will use the energy of maximal  $\bar{\nu}_e$  disappearance at KamLAND as an input in (3.16), namely,  $E_{\bar{\nu}_e}^{\text{dip}} \Big|_{\text{KamL}} \sim 3.6$  MeV. Making the additional assumption that the resonant energies  $E_{\nu_i}^{\text{res}}$  for KamLAND and T2K are the same, and using (2.35), we can recast the constraint in (3.16) as:

$$R_{m_\nu^2} \left[ \frac{|E_{\nu_2}^{\text{res}} - E_{\nu_1}^{\text{res}}|_{\text{MB}}}{\text{MeV}} \right] \lesssim 16. \quad (3.17)$$

### 3.2 Full Model — Part II: the 'vanilla' off-resonance component

We now complete the description of the full model by introducing its last component, namely, a sterile neutrino that does not couple to dark vector mediators and therefore does not experience the matter potential in (2.7). We will denote this sterile species as  $S_0$ , and will often refer to it as the *vanilla*-sterile neutrino.

In a generic UV realization of the off-resonance mechanism,  $S_0$  will mix with a linear combination of the active neutrinos,  $\nu_1$ ,  $\nu_2$ , and  $\nu_3$ , with a mixing angle  $\theta_{s_0}$ . Its purpose is to induce non-resonant oscillations that could explain the  $\bar{\nu}_e$ -like event excess at LSND and MiniBooNE, as well as the mid-energy  $\nu_e$ -like event excess at MiniBooNE, through  $\bar{\nu}_\mu \rightarrow \bar{S}_0 \rightarrow \bar{\nu}_e$  oscillations. This vanilla off-resonance mechanism will also lead to predictions for  $\bar{\nu}_\mu$  and  $\bar{\nu}_e$  disappearance in a variety of other experiments, such as MINOS, IceCube, BEST, RENO/NEOS, etc. Since the resonant and non-resonant mechanisms do not interfere in any significant way, one could in principle fit the parameters of the vanilla-sterile neutrino independently of the resonant part of the model. We will not perform this exercise in this paper, however, since our focus is on the novel part of the resonance mechanism.

Instead, we will fix the parameters of the off-resonance component to a simplified benchmark that will allow us to solve for all the propagation eigenstates *analytically*. In this simplified benchmark, the active state mixing with  $S_0$  will consist exclusively of  $\nu_1$ . Consider initially the limit in which we turn off the mixing of  $\nu_1$  with  $S_1$  (*i.e.*,  $\theta_{s_1} \rightarrow 0$ ). The two mass eigenstates would then be:

$$|\nu_1'\rangle = \cos \theta_{s_0} |\nu_1\rangle - \sin \theta_{s_0} |S_0\rangle, \quad \omega_1' \xrightarrow{\theta_{s_1} \rightarrow 0} \frac{m_1^2}{2E_\nu} \quad (3.18a)$$

$$|\nu_S\rangle = \sin \theta_{s_0} |\nu_1\rangle + \cos \theta_{s_0} |S_0\rangle, \quad \omega_0 \xrightarrow{\theta_{s_1} \rightarrow 0} \frac{M_0^2}{2E_\nu} \quad (3.18b)$$

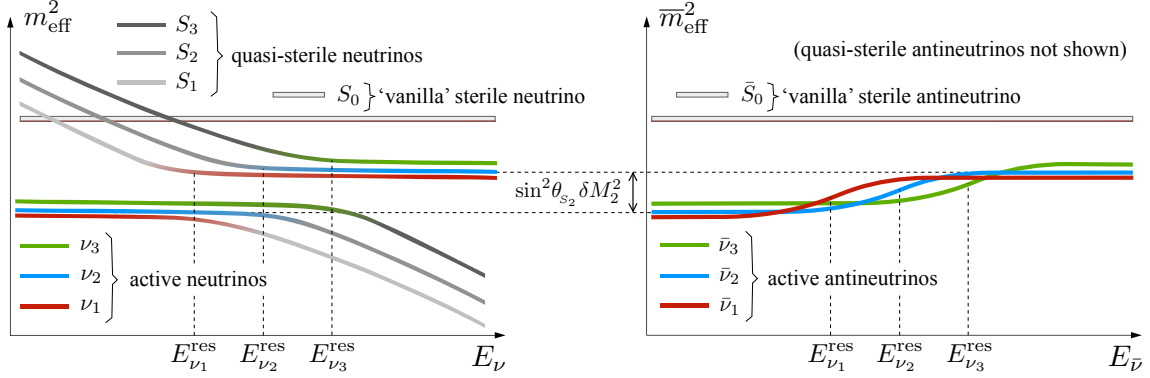


**Figure 6.** [For illustration purposes only—not to scale] Effective mass-squared eigenvalues of neutrino propagation eigenstates (left panel) and antineutrino propagation eigenstates (right panel) as a function of (anti-)neutrino energy in the full model. The eigenstates’ flavor compositions are denoted by their color shading.

The choice of  $\nu_1 - S_0$  mixing is motivated by a combination of anomalies and experimental bounds. First, since  $\nu_1$  has a significant  $\nu_e$ -component,  $\nu_1 - S_0$  mixing can easily accommodate a large (off-resonance)  $\nu_e$  disappearance rate,  $\bar{P}(\nu_e \not\rightarrow \nu_e) \approx \bar{P}(\nu_e \rightarrow S_0) = 1/2 \times |U_{e1}|^2 \sin^2 2\theta_{S_0}$ , which is convenient to address the Gallium anomalies, for instance [93–98]. Secondly,  $\nu_1$  has a smaller  $\nu_\mu$ -component than  $\nu_2$  and  $\nu_3$ , and therefore  $\nu_1 - S_0$  mixing is subject to weaker  $\bar{\nu}_\mu$  disappearance constraints from, *e.g.*, MINOS [99] and IceCube [100, 101].

Given (3.18), we could now straightforwardly turn on  $\nu_1 - S_1$  mixing. However, this would then require numerically diagonalizing the Hamiltonian for the  $\{\nu_1, S_0, S_1\}$  subsystem in order to obtain the propagation eigenstates. In order to avoid losing analytical control over our treatment, we will introduce a second simplification to our benchmark: we will mix  $S_1$  with  $\nu'_1$  in (3.18a) instead. This will allow us to retain our analytical expressions for the propagation eigenstates at arbitrary matter densities by simply making the replacement  $\nu_1 \rightarrow \nu'_1$  in (3.1), (3.2), and (3.4). This small deformation will not qualitatively affect any of the important features of the resonance mechanism. Quantitatively, we have checked that if  $S_1$  were to mix with  $\nu_1$  instead of  $\nu'_1$ , this would shift best fit parameters by  $\mathcal{O}(10\%)$ , and would also require an  $\mathcal{O}(10\%)$  adjustment of relation (3.7) in order to preserve the in-medium active neutrino mass hierarchy at high energies.

Fig. 6 illustrates the components of the full model, including the neutrino and antineutrino propagation eigenstates, their eigenvalues, and their flavor composition. The relation (3.7), combined with the fact that all active neutrinos cross the resonance within a narrow energy range, results in a much smaller deviation of the in-medium active mass spectrum relative to the SM expectation. Also, note that unlike the toy model discussed in Sec. 2, the in-medium mass hierarchy in this full model realization does not ‘flip’ at high energies.

### 3.3 Full Model — Part III: fitting the MiniBooNE low energy excess

With the full model ingredients introduced, we can recast the active neutrino flavor eigenstates in terms of the propagation eigenstates in order to derive  $\nu_\mu \rightarrow \nu_e$  oscillation probabilities for MiniBooNE. With  $\ell$  denoting active neutrino flavors ( $\ell = e, \mu, \tau$ ), we have:

$$\begin{aligned}
|\nu_\ell(L)\rangle = & \sin\theta_{S_0} U_{\ell 1}^* \left[ e^{-i\omega_0(L+\bar{L}_{\text{decay}})} |\nu_S\rangle \right] \\
& + \cos\theta_{S_0} U_{\ell 1}^* \left[ \cos\theta_{S_1}^{(m)} e^{-i\omega_1^{(-)}L} |N_{1,m}^{(-)}\rangle + \sin\theta_{S_1}^{(m)} e^{-i\omega_1^{(+)}L} |N_{1,m}^{(+)}\rangle \right] \\
& + U_{\ell 2}^* \left[ \cos\theta_{S_2}^{(m)} e^{-i\omega_2^{(-)}L} |N_{2,m}^{(-)}\rangle + \sin\theta_{S_2}^{(m)} e^{-i\omega_2^{(+)}L} |N_{2,m}^{(+)}\rangle \right] \\
& + U_{\ell 3}^* \left[ \cos\theta_{S_3}^{(m)} e^{-i\omega_3^{(-)}L} |N_{3,m}^{(-)}\rangle + \sin\theta_{S_3}^{(m)} e^{-i\omega_3^{(+)}L} |N_{3,m}^{(+)}\rangle \right].
\end{aligned} \tag{3.19}$$

Above, the matter mixing angles  $\theta_{S_i}^{(m)}$  are defined in (3.5), and the propagation eigenphases  $\omega_i^{(\pm)}$  and  $\omega_0$  are defined in (3.4) and (3.18b), respectively. As before, we take MiniBooNE's propagation length  $L$  to be the average distance through which neutrinos travel in matter,  $L \approx 490$  m, and we assume constant matter density and earth composition throughout<sup>3</sup>. The additional ‘averaged decay baseline’  $\bar{L}_{\text{decay}}$  appearing in the first line of (3.19) is an approximation to account for the state's evolution within the decay region of the BNB beamline, which for simplicity we take to be  $\bar{L}_{\text{decay}} \sim 30$  m. Only the phase of the  $\nu_S$  component of  $\nu_\ell$  changes non-negligibly within the decay region (see (3.18)); therefore, the phase change of the  $\nu_1'$  component within the decay region is ignored in (3.19).

Given the relations (3.3), (3.7), and (3.10), we can fully specify all the parameters of the full model by a set of 7 independent parameters: 5 related to the triple-resonance mechanism, which we choose to be  $\theta_{S_2}$ ,  $R_{m_2^2}$ ,  $E_{\nu_1}^{\text{res}}$ ,  $E_{\nu_2}^{\text{res}}$ ,  $E_{\nu_3}^{\text{res}}$ ; and 2 related to the off-resonance oscillations,  $\theta_{S_0}$  and  $M_0^2$ .

In fitting MiniBooNE's  $\nu_e$  appearance data, we will fix the off-resonance parameters to the following (non-optimized) values<sup>4</sup>:

$$\theta_{S_0} = 0.30 \quad , \quad M_0^2 = 1.0 \text{ eV}^2. \tag{3.20}$$

As for the parameters of the triple-resonance mechanism, we have found that if either  $E_{\nu_1}^{\text{res}}$  or  $E_{\nu_2}^{\text{res}}$  is within  $\mathcal{O}(20\%)$  of  $\sim 300$  MeV, the full model can provide excellent fits to MiniBooNE's data while simultaneously satisfying the constraints in (3.11), (3.15), and

<sup>3</sup>In particular, we neglect possible effects of other structures in the neutrino's propagation path, such as the steel and concrete beam absorber, vault and detector walls, the mineral oil target before interaction, etc.

<sup>4</sup>This choice of off-resonance parameters is motivated by the Gallium  $\nu_e$  disappearance anomalies [93–98], including the most recent results from the BEST collaboration [102]. However, we note that these parameters are in strong tension with more recent oscillation bounds from reactor-based antineutrino experiments [103], such as the combined results from RENO and NEOS [104]. Notwithstanding, the  $\nu_e$  spectral shape at RENO, NEOS, and other reactor experiments (Daya Bay, Double Chooz) shows a significant departure from flux models' expectations at energies around  $\sim 5 - 6$  MeV, whose origin is not understood [105–111]. We speculate that there might be additional systematic uncertainties in reactor antineutrino measurements that have not been accounted for [112–115]; therefore, we choose to ignore reactor-based constraints on ‘3+1’ sterile neutrino models [116–119].

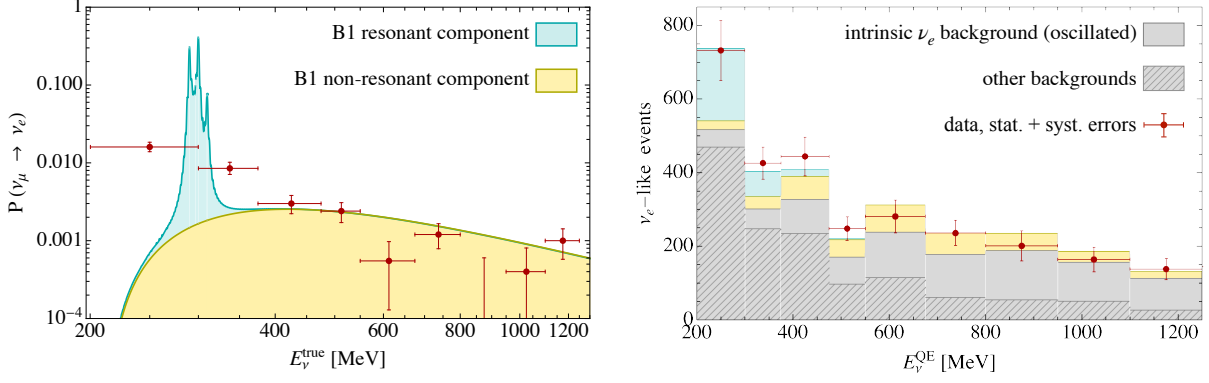


**Figure 7.** Left panel: the  $\nu_\mu \rightarrow \nu_e$  appearance probability at MiniBooNE predicted by the benchmark model B1 specified in (3.20, 3.22a). The non-resonant component (yellow region) is the expectation from this model if the triple-resonance mechanism were ‘turned off’ (*i.e.*, if the active-quasi-sterile mixing angles  $\theta_{s_1}, \theta_{s_2}, \theta_{s_3}$  were set to zero). The red data points with error bars were taken from Fig. 21 of [22]; they assume  $E_\nu^{\text{true}} \sim E_\nu^{\text{QE}}$ , which is a very coarse approximation. As such, they should be interpreted as a *qualitative* measure of MiniBooNE’s anomalous appearance probabilities. Right panel: The expected  $\nu_e$  appearance event rate at MiniBooNE predicted by the full model benchmark B1. The intrinsic (beam)  $\nu_e$  component of the background takes  $\nu_e \nrightarrow \nu_e$  oscillations into account. The red data points correspond to the measurements reported by MiniBooNE in [22], and the error bars include both statistical and systematic uncertainties.

(3.17). These excellent fits (*i.e.*, within  $1\sigma$  of the best-fit point) are achieved if the mixing angle  $\theta_{s_j}$  associated with the resonant energy  $E_{\nu_j}^{\text{res}}$  closest to  $\sim 300$  MeV satisfies the condition of appearance probability saturation at the resonance, analogous to (2.32):

$$\begin{aligned} \sin \theta_{s_j} &\lesssim |\sin \theta_{s_j}^{\text{(max)}}| = \frac{R_{m_\nu^2} |\delta m_{32}^2|}{2\pi} \frac{L}{E_{\nu_j}^{\text{res}}} \Bigg|_{\text{MB}} \\ &\lesssim 3.3 \times 10^{-3} R_{m_\nu^2} \frac{(300 \text{ MeV})}{E_{\nu_j}^{\text{res}} \Big|_{\text{MB}}}. \end{aligned} \quad (3.21)$$

Figs. 7 and 8 (left panels) show the  $\nu_\mu \rightarrow \nu_e$  appearance probability at MiniBooNE as a function of true neutrino energy for two illustrative benchmark points:

$$\text{B1: } \theta_{s_2} = \mathbf{0.003}, R_{m_\nu^2} = 0.9, E_{\nu_1}^{\text{res}} = 290 \text{ MeV}, E_{\nu_2}^{\text{res}} = 300 \text{ MeV}, E_{\nu_3}^{\text{res}} = 310 \text{ MeV}, \quad (3.22a)$$

$$\text{B2: } \theta_{s_2} = \mathbf{0.006}, R_{m_\nu^2} = 0.9, E_{\nu_1}^{\text{res}} = 290 \text{ MeV}, E_{\nu_2}^{\text{res}} = 300 \text{ MeV}, E_{\nu_3}^{\text{res}} = 310 \text{ MeV}, \quad (3.22b)$$

with the off-resonance parameters set to the values in (3.20). The right panels in Figs. 7 and 8 show the expected contribution of these two benchmarks to the MiniBooNE  $\nu_e$  event spectrum. These rates were obtained using the information provided by the MiniBooNE collaboration in its 2021 public data release [120], and include the effects of oscillations of the intrinsic  $\nu_e$  background from the Booster Neutrino Beam (BNB). Note that even for

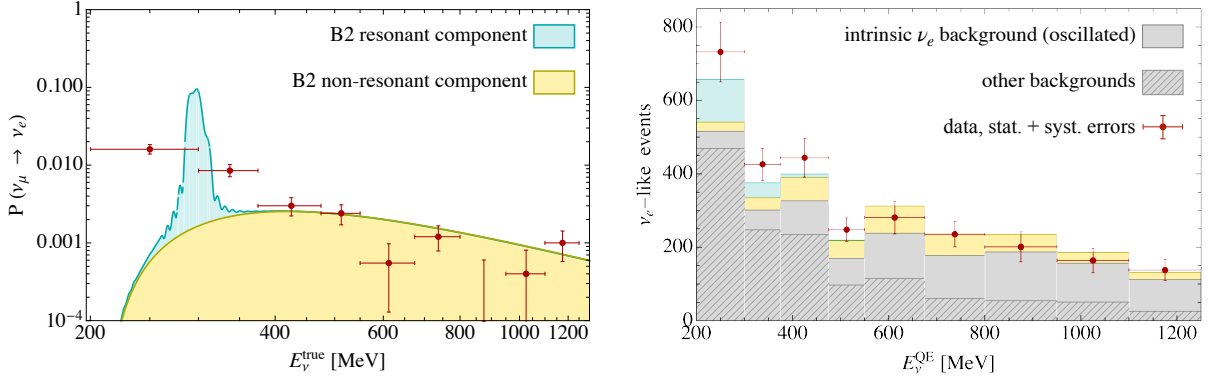


**Figure 8.** Same as in Fig. 7 but for the benchmark model B2 specified in (3.20, 3.22b).

benchmark B2 in (3.22b), which lies outside the appearance probability saturation range in (3.21), the triple-resonance mechanism provides an adequate fit to the MiniBooNE  $\nu_e$ -like excess, as can be seen from Figs. 8 (left panel).

At this point, it is germane to comment on the  $\cos\theta_e$  distribution of MiniBooNE’s excess events ( $\theta_e$  is defined as the angle of the reconstructed electron relative to the neutrino beam). The  $\cos\theta_e$  spectral shape of the MiniBooNE excess appears to be more forward-peaked in the region  $\cos\theta_e > 0.9$  than what is expected from the kinematics of  $\nu_e$  charged-current quasi-elastic (CCQE) scattering, but not forward enough to be consistent with  $\nu - e^-$  elastic scattering. In fact, the forward excess in  $\cos\theta_e > 0.9$  has motivated many non-oscillatory interpretations of the MiniBooNE anomaly. Indeed, if statistically significant, this spectral feature could in principle rule out explanations of the  $\nu_e$ -like excess based on *bona fide*  $\nu_e$  appearance. However, we note that the MiniBooNE collaboration has not performed any studies to quantify the experimental systematics associated with the  $\cos\theta_e$  distribution (and, in fact, MiniBooNE’s modeling of the  $\nu_e$  backgrounds in the forward low energy kinematic region has limited statistics). Hence, at present one cannot rule out the  $\nu_e$  CCQE scattering hypothesis for the MiniBooNE excess based on its  $\cos\theta_e$  event distribution.

Finally, in Fig. 9 we show the effective active mass-squared splittings  $\delta m_{32, \text{eff}}^2$ ,  $\delta \bar{m}_{31, \text{eff}}^2$ , and  $\delta \bar{m}_{21, \text{eff}}^2$  as a function of (anti-)neutrino energy for the benchmarks in (3.22). The rapid relaxation of these active mass-squared splittings towards their SM expectation indicates that the triple-resonance mechanism, unlike the models discussed in [53, 54, 56, 59], can explain the MiniBooNE excess while remaining compatible with observations from long-baseline neutrino experiments.

#### 4 Further implications of quasi-sterile neutrinos and BSM matter effects

There are other experimental observations that could be significantly impacted by the resonant mechanism of quasi-sterile neutrinos, and in particular by the specific realization considered in Sec. 3 to explain the MiniBooNE and LSND anomalies. Two obvious issues are

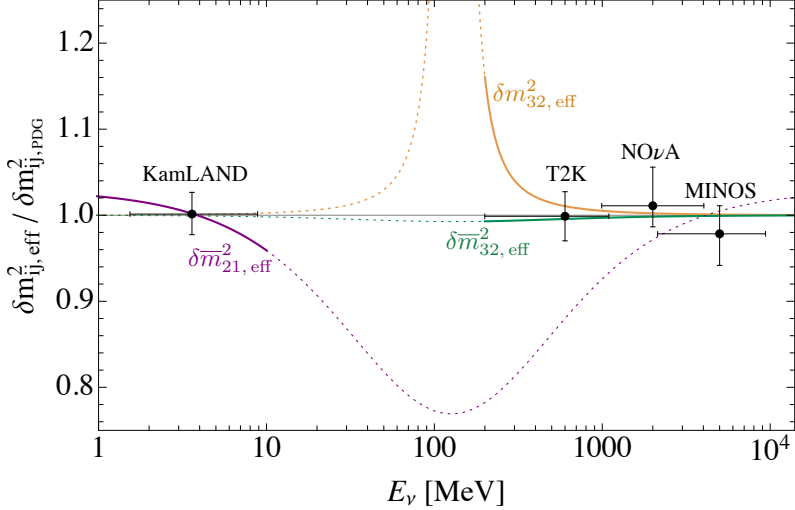


**Figure 9.** Effective mass-squared splittings  $\delta m_{ij,\text{eff}}^2$  predicted by the full model benchmarks B1 and B2 in (3.22) as a function of (anti-)neutrino energy (both benchmarks’ predictions are indistinguishable as displayed in this plot). All effective mass-squared splittings shown have been normalized to the appropriate central value  $\delta m_{ij,\text{PDG}}^2$  reported in the PDG [62]. Solid purple curve: the effective ‘solar’ mass-squared splitting for antineutrinos,  $\delta \bar{m}_{21,\text{eff}}^2$ , expected at KamLAND. Solid orange (green) curve: the effective ‘atmospheric’ mass-squared splitting for neutrinos (antineutrinos),  $\delta m_{32,\text{eff}}^2$  ( $\delta \bar{m}_{32,\text{eff}}^2$ ), expected at long-baseline accelerator neutrino experiments running in neutrino (antineutrino) mode. The dotted parts of these curves indicate energy ranges that have not been experimentally probed. The data points with error bars denote recent measurements of  $\delta \bar{m}_{21,\text{eff}}^2$ ,  $\delta m_{32,\text{eff}}^2$ , and  $\delta \bar{m}_{32,\text{eff}}^2$  by long-baseline experiments [79–81, 92].

(i) the implications for solar neutrinos, and (ii) the expected BSM  $\nu_e$  flux at MicroBooNE, which is of significant relevance at present in light of the recent results reported by the MicroBooNE collaboration in [61]. In this section we briefly comment on generic experimental implications of the triple-resonance mechanism for solar neutrinos and MicroBooNE, while deferring a comprehensive investigation of these issues to a future publication [15].

#### 4.1 Implications for MicroBooNE

The MicroBooNE collaboration recently released the results of three searches for  $\nu_e$  scattering events based on data obtained with Fermilab’s BNB in neutrino-mode from an exposure of  $7 \times 10^{20}$  POT [121–123]. These analyses targeted independent final states of  $\nu_e$ -nuclear scattering: the ‘Wire-Cell’ search in [121] was fully inclusive in all possible hadronic final states; the ‘Deep-Learning’ search in [122] selected exclusive two-body  $e^-p$  final states to obtain increased sensitivity to  $\nu_e$  CCQE scattering; and the semi-inclusive ‘Pandora’ search in [123] applied a pion veto on its selection of  $e^- + Np$  final states ( $N \geq 0$ ). The non-observation of an excess of events in these searches (and, in fact, the observation of a *deficit* of events in the inclusive Wire-Cell and CCQE Deep-Learning searches) allowed MicroBooNE to exclude an *ad hoc* parametrization of the MiniBooNE low energy excess, coined the ‘eLEE’ model, at a confidence level greater than  $\sim 97\%$ .

While at face value these results appear to strongly disfavor  $\nu_e$  appearance interpretations of the MiniBooNE low energy excess, we contend that such a general conclusion is premature. In particular, we highlight several caveats that could invalidate the generality of MicroBooNE’s exclusion of  $\nu_\mu \rightarrow \nu_e$  oscillation hypotheses addressing the MiniBooNE anomaly:

1. The observed  $\nu_e$  rates in the MicroBooNE BNB data were significantly lower than the background expectation for the three most sensitive channels—the CCQE Deep-Learning search, for example, found a  $p$ -value of  $p = 0.014$  for the background-only hypothesis. This led to stronger than expected exclusions of the eLEE model signal strength. Assuming this discrepancy between data and background expectation was due to a downward statistical fluctuation, it is likely that more data will lead to a weakening of MicroBooNE’s constraints. On the other hand, if tensions persist with more data, this would point to a possible mismodelling of expected backgrounds, which would require a revision of the MicroBooNE bounds. Either way, it is unlikely that upcoming MicroBooNE analyses with twice as much beam luminosity will lead to tighter bounds on models predicting BSM  $\nu_e$  appearance at MiniBooNE and MicroBooNE.
2. The MicroBooNE analyses tested only the very specific eLEE model, which was an *ad hoc*  $\nu_e$  excess flux obtained by ‘reverse-engineering’ the MiniBooNE  $\nu_e$ -like excess. The MicroBooNE collaboration chose to normalize the eLEE flux relative to the *intrinsic*  $\nu_e$  flux (*i.e.*, the background  $\nu_e$  component in the BNB originating from decays of muons and kaons produced at the source). Fig. 10 shows the expected eLEE  $\nu_e$  spectrum at MicroBooNE taken from Fig. 2 of [122]; for each energy bin, the eLEE flux is weighted relative to the intrinsic  $\nu_e$  flux integrated over that same bin. The fact that the reported MicroBooNE exclusions were cast in terms of the eLEE signal strength constitutes perhaps the most important caveat concerning these results: *the mapping of the MiniBooNE excess to a truth-level  $\nu_e$  spectrum is not injective*, and in fact other  $\nu_e$  spectra departing considerably from the eLEE model can also provide good fits to the MiniBooNE excess (see also [124]). We will come back to this point shortly.
3. The MicroBooNE analyses assumed that the eLEE  $\nu_e$  flux, when normalized to the intrinsic  $\nu_e$  flux, was identical at MiniBooNE and MicroBooNE. This simplified assumption fails to capture important features of BSM oscillation models. For instance, the fact that MicroBooNE’s baseline is about 70 m shorter than MiniBooNE’s could have a non-negligible effect on  $\nu_\mu \rightarrow \nu_e$  oscillation probabilities. Furthermore, intrinsic  $\nu_e$  disappearance could be non-negligible at MicroBooNE (see also [125]), especially if the Gallium anomalies are indeed an indication of large  $\nu_e$  disappearance at  $L/E_{\nu_e} \sim \mathcal{O}(\text{m/MeV})$ . In this case, MicroBooNE’s constraints on a realistic oscillation model would be less severe than those implied from the eLEE signal strength due to a reduction of the intrinsic  $\nu_e$  backgrounds. (Note that a non-negligible  $\nu_e$  disappearance probability would not be as consequential for the MiniBooNE excess

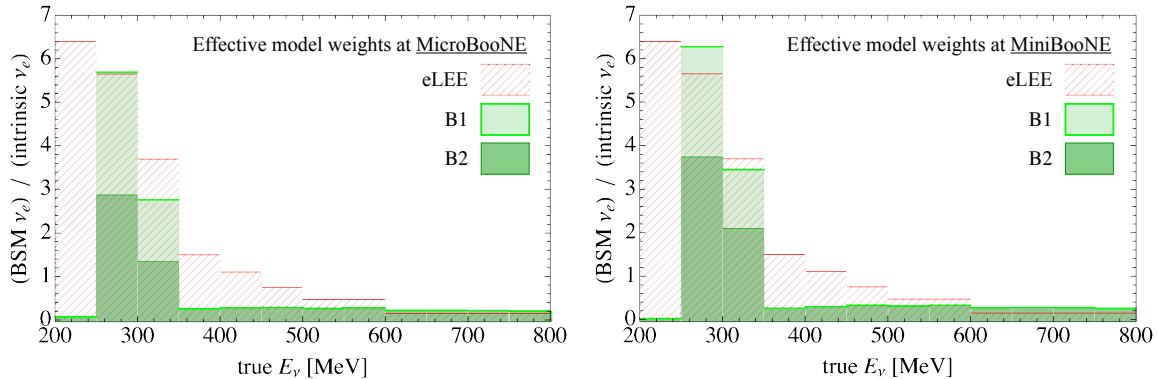


**Figure 10.** The *effective* BSM  $\nu_e$  fluxes at the MicroBooNE (left) and MiniBooNE (right) detectors from the BNB normalized by the expected intrinsic  $\nu_e$  background flux in the SM, as predicted by three different models: the *ad hoc* eLEE model used in the MicroBooNE analyses (red hatched histogram); the quasi-sterile benchmark model B1 in (3.22a) and Fig. 7 (light green histogram); and the quasi-sterile benchmark model B2 in (3.22b) and Fig. 8 (dark green histogram). For B1 and B2, the ‘effective’ BSM  $\nu_e$  fluxes include  $\nu_\mu \rightarrow \nu_e$  oscillations as well as intrinsic  $\nu_e$  disappearance.

because the backgrounds from intrinsic  $\nu_e$  CCQE scattering events at MiniBooNE are sub-dominant in the low energy region  $E_\nu|_{\text{MB}} \lesssim 400$  MeV.)

The triple-resonance model presented in Sec. 3 provides a clear example of caveats 2 and 3 above. Fig. 10 (left panel) contrasts the eLEE  $\nu_e$  flux at MicroBooNE with the *effective*  $\nu_e$  flux predicted by the quasi-sterile benchmarks B1 and B2 specified in (3.20) and (3.22a, 3.22b). In order to provide an ‘apples-to-apples’ comparison with the eLEE model, the effective  $\nu_e$  fluxes for B1 and B2 shown in Fig. 10 include not only  $\nu_\mu \rightarrow \nu_e$  appearance, but also intrinsic  $\nu_e$  disappearance (which is predominantly due to  $\nu_e$ -to-sterile oscillations with an averaged disappearance probability of  $\bar{P}_{\nu_e \rightarrow S_0} \approx 1/2 \times |U_{e1}|^2 \sin^2 2\theta_{S_0} \approx 11\%$  away from the resonant region). The effects of  $\nu_\mu$  disappearance, which would affect the normalization of the  $\nu_\mu$  flux and consequently the constrained  $\nu_e$  predictions, have been ignored. These effects are small away from the resonance, where they are dominated by  $\nu_\mu$ -to-sterile oscillations with an averaged  $\nu_\mu$  disappearance probability of  $\bar{P}_{\nu_\mu \rightarrow S_0} \approx 1/2 \times |U_{\mu 1}|^2 \sin^2 2\theta_{S_0} \approx 2\%$ . Around the resonant region,  $\nu_\mu$  disappearance is more significant—averaging to  $\mathcal{O}(10\%)$  for the benchmarks B1 and B2—but still within the  $\nu_\mu$  flux uncertainty at MicroBooNE. A more comprehensive study including the effects of  $\nu_\mu$  disappearance are deferred to a future study.

Fig. 10 (right panel) contrasts the eLEE, B1, and B2 predictions for the BSM  $\nu_e$  flux at MiniBooNE normalized to the intrinsic  $\nu_e$  flux. We can compare these predictions with the ones for MicroBooNE shown in the left panel: while the eLEE prediction is, by definition, identical at MicroBooNE and MiniBooNE, the predictions from the B1 and B2 quasi-sterile benchmarks are qualitatively different. This is due to the difference in baselines between MicroBooNE and MiniBooNE mentioned in caveat 3 above. In particular, this difference is more pronounced for B2 because this benchmark does not saturate the appearance prob-

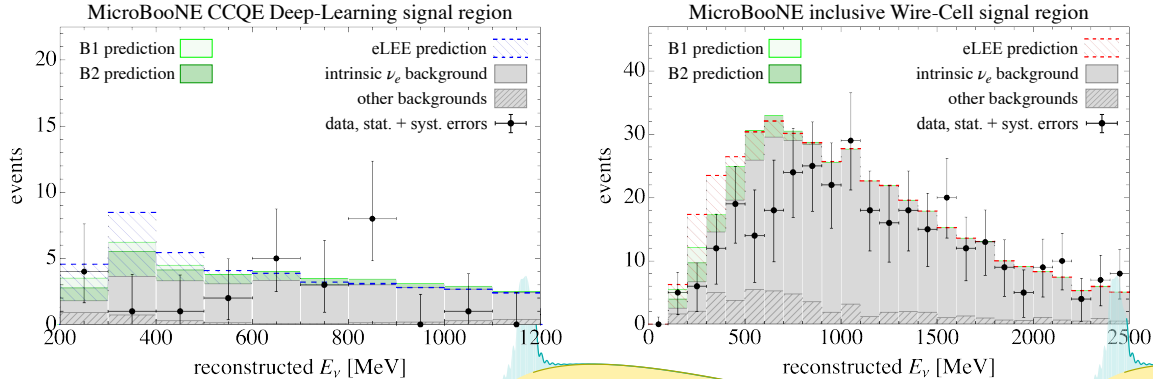


**Figure 11.** Expected  $\nu_e$  event rates for two MicroBooNE searches: the CCQE Deep-Learning [122] (left) and the inclusive Wire-Cell [121] (right) signal regions. The gray histograms denote the expected backgrounds obtained by the MicroBooNE collaboration in each analysis. In particular, the intrinsic  $\nu_e$  background rate is the one expected in the SM and does not assume BSM  $\nu_e$  oscillations. The blue hatched histogram is the  $\nu_e$  event rate prediction from the eLEE model used in the MicroBooNE analyses. The light and dark green histograms denote approximate  $\nu_e$  event rate predictions from the B1 and B2 quasi-sterile benchmarks (see text for details). Since intrinsic  $\nu_e$  disappearance has not been included in the background histograms, this effect has been absorbed in the green histograms for the B1 and B2 predictions. The data error bars include statistical and systematic uncertainties.

ability at the resonance, and MicroBooNE’s shorter baseline takes the  $\nu_\mu \rightarrow \nu_e$  oscillation probability further away from the saturation condition relative to MiniBooNE (see (3.21) and discussion around it).

It is difficult, however, to draw any firm conclusion from the comparisons of truth-level  $\nu_e$  rate predictions shown in Fig. 10. Smearing and bias effects in energy reconstruction, and the rapid reduction of event selection efficiency towards lower energies, make it non-trivial to infer which part of the  $\nu_e$  signal spectrum dominates the expected  $\nu_e$  event rates in the various MicroBooNE analyses. Unlike MiniBooNE’s public data releases, the MicroBooNE collaboration has not released sufficient information to allow one to perform an end-to-end statistical analysis of the consistency of an *arbitrary* oscillation model with the MicroBooNE data.

The public data release for the CCQE Deep-Learning analysis [126], for instance, provided a Monte Carlo  $\nu_e$  event sample [127] that can be re-weighted to obtain *unconstrained*  $\nu_e$  event rate predictions from an arbitrary model. Using these tools, we have obtained the unconstrained  $\nu_e$  event rate predicted by the B1 and B2 benchmarks in the CCQE Deep-Learning signal region. However, with the information in the public data release alone, we cannot proceed beyond this point. Specifically, no tools were provided to construct the full covariance matrix for an arbitrary model; without it, one cannot obtain the *constrained*  $\nu_e$  event rate prediction, nor its associated  $p$ -value. Given these limitations, we instead took a heuristic approach: we inferred a bin-by-bin re-weighting procedure that reproduced the constrained  $\nu_e$  rates given in [128]. We applied this same re-weighting procedure to our B1

and B2 benchmarks to obtain their expected constrained  $\nu_e$  rates, shown in Fig. 11 (right panel). While we still could not obtain their corresponding  $p$ -values without a covariance matrix, inspection of Fig. 11 (right) allows us to at least draw a qualitative conclusion from it: the predictions from quasi-sterile benchmark models are in significantly less tension with MicroBooNE’s data than the eLEE model’s prediction. Indeed, it is possible that these benchmarks are not incompatible with observations at a high enough confidence level to be excluded.

As for the inclusive Wire-Cell analysis, its public data release to date [129] provided smearing tables to map true neutrino energy into reconstructed neutrino energy [130], as well as event selection efficiencies as a function of true neutrino energy [131], which in principle would allow one to obtain the unconstrained  $\nu_e$  event rate for an arbitrary model. However, similarly to the public data release for the CCQE Deep-Learning analysis, no tools were provided to allow one to construct the covariance matrix for such an arbitrary model, without which one cannot obtain the constrained  $\nu_e$  event rate. Furthermore, the event selection efficiencies provided in the public data release were binned too coarsely in the low energy region to be useful. Therefore, here too we resorted to a semi-heuristic bin re-weighting procedure that reproduced the binned ratio of fully contained, constrained event rate predictions [132] for the eLEE model relative to the intrinsic  $\nu_e$  backgrounds. In Fig. 11 (right panel) we show the expected events rates in the inclusive Wire-Cell signal region obtained from applying this semi-heuristic procedure to the B1 and B2 benchmarks. Again, without the means to obtain the covariance matrices for these benchmark models, we could not estimate a  $p$ -value for the B1 and B2 predictions shown in Fig. 11 (right). However, our prior qualitative conclusion from the CCQE Deep-Learning analysis is not contradicted here: the quasi-sterile oscillation model can provide a good explanation for the MiniBooNE excess while being consistent with the recent constraints from MicroBooNE. Further data will hopefully make this situation less ambiguous.

## 4.2 Implications for solar neutrinos

The triple-resonance mechanism that explains the MiniBooNE excess should considerably alter neutrino propagation and flavor conversion in the Sun. Several compounding effects come into play. First, the quasi-sterile resonant energies in the solar core are expected to fall in the range  $E_{\nu_i}^{\text{res}}|_{\odot} \sim \mathcal{O}(\rho_{\text{MB}}/\rho_{\odot}) E_{\nu_i}^{\text{res}}|_{\text{MB}} \sim \mathcal{O}(\text{MeV})$ , which is of the same magnitude as the resonant energy of the standard MSW effect. Second, in the vicinity of the resonant energies  $E_{\nu_{1,2}}^{\text{res}}|_{\odot}$ , the effective active mass-squared splitting  $\delta m_{21,\text{eff}}^2$  in the solar medium will deviate by  $\mathcal{O}(1-10)$  from the SM expectation, hence altering the MSW effect itself. Third, the quasi-sterile neutrinos  $S_i$  ( $i = 1, 2, 3$ ) could have short mean-free-paths in the solar medium due to their vector portal interactions with ordinary matter; this would cause decoherence of superpositions of active and quasi-sterile neutrino states.

However, precise predictions can only be made once a concrete model is specified for dark vector mediator responsible for the BSM matter potential. In particular, the quasi-sterile resonant energies in the solar core will depend not only on the ratio of dirt-to-solar core densities,  $\rho_{\text{MB}}/\rho_{\odot}$ , but also on the specific couplings of the dark mediator to electrons, neutrons, and protons, since the relative neutron-to-proton and nucleon-to-electron compo-

sitions in the solar core differ by  $\mathcal{O}(1)$  from the shallow Earth crust composition through which neutrinos propagate in accelerator experiments. In addition, in order to compute the quasi-sterile neutrinos' mean-free-path in the solar medium, the mediator's mass and couplings are needed. Finally, the model-dependent solar emission of quasi-sterile neutrinos could lead to scattering signals in neutrino and dark matter experiments such as SK, SNO, Borexino, and XENON1T (see also [133–136]).

Our preliminary investigations indicate that it is possible to build a dark sector UV completion that is experimentally viable and leads to predictions compatible with existing solar neutrino data. This is however beyond the scope of this work; a complete study of implications of this model to active and quasi-sterile solar neutrinos will appear in a follow-up paper [15].

## 5 Summary and Outlook

An inevitable consequence of dark sector models with quasi-sterile neutrinos are new matter effects in neutrino propagation through a medium, which can lead to two generic effects. The first is resonant active-to-sterile neutrino oscillations around a resonant energy  $E_\nu^{\text{res}}$  determined by the medium's forward scattering potential. This effect occurs for either neutrinos or antineutrinos, but not both, and the choice is determined by the sign of the effective matter potential. The second effect, which affects both neutrinos and antineutrinos, is an energy- and medium-dependent modification of the active neutrino mass spectrum. This modification disappears in the asymptotic limits  $E_\nu \ll E_\nu^{\text{res}}$  and  $E_\nu \gg E_\nu^{\text{res}}$ , but becomes increasingly pronounced as  $E_\nu$  approaches the resonant energy. Generic realizations of these effects are obviously not phenomenologically viable given the swath of experimental measurements targeting different neutrino flavors, energies, and baselines.

In this paper, we have studied a specific realization of a model with quasi-sterile neutrinos and resonant oscillations that can address the short-baseline  $\nu_\mu \rightarrow \nu_e$  anomalies while preserving the effective neutrino mass spectrum in regimes probed by long-baseline experiments. We have also argued that the recent  $\nu_e$  measurements by MicroBooNE likely do not exclude this model. Additional data from MicroBooNE expected in the near future is unlikely to unambiguously resolve the initial tensions between prediction and observations; however, in the longer term, the SBN program, including MicroBooNE, SBND, and ICARUS, will be able to fully test our proposed explanation for the MiniBooNE and LSND anomalies.

Further, while this model can accommodate non-negligible  $\bar{\nu}_e$  disappearance probabilities, it does not address the significant tensions between the existing  $\bar{\nu}_e$  disappearance measurements. Proposed experiments such as IsoDAR@Yemilab [137, 138] will be rid of large systematic flux uncertainties, and will be able to reconstruct the antineutrino's energy and propagated distance with high precision on an event-by-event basis. As such, it should be able to resolve the ambiguities and inconsistencies that currently plague the  $\bar{\nu}_e$  disappearance experimental landscape. Being an *antineutrino* experiment, IsoDAR@Yemilab will not be able to probe the resonant mechanism within the model proposed in this study;

nonetheless, it will be able to test this model through its non-resonant  $\bar{\nu}_e$  oscillation predictions.

The resonant mechanism of this quasi-sterile neutrino model should also have significant consequences for solar neutrinos, and offer testable predictions for active solar neutrino emission, as well as quasi-sterile solar neutrino emission which could lead to distinct signals in dark matter and solar neutrino experiments. A comprehensive study of the BSM solar neutrino phenomenology in this context is deferred to a future publication [15].

## Acknowledgments

DSMA benefited from conversations with the late Ann Nelson on model building aspects of this study; Ann is sorely missed. DSMA also acknowledges the Aspen Center for Physics (ACP) where this work was partially developed—the ACP is supported by National Science Foundation grant PHY-1607611. We are grateful to En-Chuan Huang for useful explanations regarding the MiniBooNE data, and Janet Conrad and Mark Ross-Lonergan for discussions regarding the recent MicroBooNE analyses. This work was supported by the Los Alamos National Laboratory LDRD program, and by the DOE Office of Science High Energy Physics under contract number DE-AC52-06NA25396.

## References

- [1] N. Arkani-Hamed, D. P. Finkbeiner, T. R. Slatyer and N. Weiner, *A Theory of Dark Matter*, *Phys. Rev. D* **79** (2009) 015014 [[0810.0713](#)].
- [2] J. Jaeckel and A. Ringwald, *The Low-Energy Frontier of Particle Physics*, *Ann. Rev. Nucl. Part. Sci.* **60** (2010) 405 [[1002.0329](#)].
- [3] R. Essig et al., *Working Group Report: New Light Weakly Coupled Particles*, in *Community Summer Study 2013: Snowmass on the Mississippi*, 10, 2013, [1311.0029](#).
- [4] J. Alexander et al., *Dark Sectors 2016 Workshop: Community Report*, 8, 2016, [1608.08632](#).
- [5] G. Lanfranchi, M. Pospelov and P. Schuster, *The Search for Feebly-Interacting Particles*, [2011.02157](#).
- [6] XENON collaboration, *Excess electronic recoil events in XENON1T*, *Phys. Rev. D* **102** (2020) 072004 [[2006.09721](#)].
- [7] A. H. Córscico, L. G. Althaus, M. M. Miller Bertolami, S. O. Kepler and E. García-Berro, *Constraining the neutrino magnetic dipole moment from white dwarf pulsations*, *JCAP* **08** (2014) 054 [[1406.6034](#)].
- [8] S. Arceo Díaz, K.-P. Schröder, K. Zuber, D. Jack and E. E. Bricio Barrios, *Constraint on the axion-electron coupling constant and the neutrino magnetic dipole moment by using the tip-RGB luminosity of fifty globular clusters*, *arXiv e-prints* (2019) arXiv:1910.10568 [[1910.10568](#)].
- [9] N. Yusof, H. A. Kassim, L. G. Garba and N. S. Ahmad, *The neutrino emission from thermal processes in very massive stars in the local universe*, *Mon. Not. Roy. Astron. Soc.* **503** (2021) 5965 [[2103.07069](#)].

- [10] A. Studenikin, *Electromagnetic neutrino: The basic processes and astrophysical probes*, in *17th International Conference on Topics in Astroparticle and Underground Physics*, 10, 2021, [2111.00469](#).
- [11] C. Boehm, D. G. Cerdeno, M. Fairbairn, P. A. N. Machado and A. C. Vincent, *Light new physics in XENON1T*, *Phys. Rev. D* **102** (2020) 115013 [[2006.11250](#)].
- [12] I. M. Bloch, A. Caputo, R. Essig, D. Redigolo, M. Sholapurkar and T. Volansky, *Exploring new physics with  $O(\text{keV})$  electron recoils in direct detection experiments*, *JHEP* **01** (2021) 178 [[2006.14521](#)].
- [13] K. S. Babu, S. Jana and M. Lindner, *Large Neutrino Magnetic Moments in the Light of Recent Experiments*, *JHEP* **10** (2020) 040 [[2007.04291](#)].
- [14] S.-F. Ge, P. Pasquini and J. Sheng, *Solar Active-Sterile Neutrino Conversion with Atomic Effects at Dark Matter Direct Detection Experiments*, [2112.05560](#).
- [15] D. S. M. Alves, W. C. Louis and P. deNiverville, *Quasi-Sterile Neutrinos from Dark Sectors — II. Dark mediator phenomenology*, [To appear](#).
- [16] LSND collaboration, *Evidence for anti-muon-neutrino  $\rightarrow$  anti-electron-neutrino oscillations from the LSND experiment at LAMPF*, *Phys. Rev. Lett.* **77** (1996) 3082 [[nucl-ex/9605003](#)].
- [17] LSND collaboration, *Evidence for  $\nu(\mu) \rightarrow \nu(e)$  neutrino oscillations from LSND*, *Phys. Rev. Lett.* **81** (1998) 1774 [[nucl-ex/9709006](#)].
- [18] LSND collaboration, *Evidence for neutrino oscillations from muon decay at rest*, *Phys. Rev. C* **54** (1996) 2685 [[nucl-ex/9605001](#)].
- [19] LSND collaboration, *Evidence for muon-neutrino  $\rightarrow$  electron-neutrino oscillations from pion decay in flight neutrinos*, *Phys. Rev. C* **58** (1998) 2489 [[nucl-ex/9706006](#)].
- [20] LSND collaboration, *Evidence for neutrino oscillations from the observation of  $\bar{\nu}_e$  appearance in a  $\bar{\nu}_\mu$  beam*, *Phys. Rev. D* **64** (2001) 112007 [[hep-ex/0104049](#)].
- [21] MINIBOONE collaboration, *Significant Excess of ElectronLike Events in the MiniBooNE Short-Baseline Neutrino Experiment*, *Phys. Rev. Lett.* **121** (2018) 221801 [[1805.12028](#)].
- [22] MINIBOONE collaboration, *Updated MiniBooNE neutrino oscillation results with increased data and new background studies*, *Phys. Rev. D* **103** (2021) 052002 [[2006.16883](#)].
- [23] MICROBOONE collaboration, *Search for Neutrino-Induced Neutral Current  $\Delta$  Radiative Decay in MicroBooNE and a First Test of the MiniBooNE Low Energy Excess Under a Single-Photon Hypothesis*, [2110.00409](#).
- [24] R. J. Hill, *On the single photon background to  $\nu_e$  appearance at MiniBooNE*, *Phys. Rev. D* **84** (2011) 017501 [[1002.4215](#)].
- [25] X. Zhang and B. D. Serot, *Can neutrino-induced photon production explain the low energy excess in MiniBooNE?*, *Phys. Lett. B* **719** (2013) 409 [[1210.3610](#)].
- [26] E. Wang, L. Alvarez-Ruso and J. Nieves, *Photon emission in neutral current interactions at intermediate energies*, *Phys. Rev. C* **89** (2014) 015503 [[1311.2151](#)].
- [27] E. Wang, L. Alvarez-Ruso and J. Nieves, *Single photon events from neutral current interactions at MiniBooNE*, *Phys. Lett. B* **740** (2015) 16 [[1407.6060](#)].
- [28] L. Alvarez-Ruso and E. Saul-Sala, *Neutrino Interactions with Matter and the MiniBooNE anomaly*, [2111.02504](#).

- [29] M. Maltoni, T. Schwetz, M. A. Tortola and J. W. F. Valle, *Ruling out four neutrino oscillation interpretations of the LSND anomaly?*, *Nucl. Phys. B* **643** (2002) 321 [[hep-ph/0207157](#)].
- [30] M. Maltoni and T. Schwetz, *Sterile neutrino oscillations after first MiniBooNE results*, *Phys. Rev. D* **76** (2007) 093005 [[0705.0107](#)].
- [31] J. M. Conrad, C. M. Ignarra, G. Karagiorgi, M. H. Shaevitz and J. Spitz, *Sterile Neutrino Fits to Short Baseline Neutrino Oscillation Measurements*, *Adv. High Energy Phys.* **2013** (2013) 163897 [[1207.4765](#)].
- [32] J. Kopp, P. A. N. Machado, M. Maltoni and T. Schwetz, *Sterile Neutrino Oscillations: The Global Picture*, *JHEP* **05** (2013) 050 [[1303.3011](#)].
- [33] C. Giunti and E. M. Zavanin, *Appearance-disappearance relation in  $3 + N_s$  short-baseline neutrino oscillations*, *Mod. Phys. Lett. A* **31** (2015) 1650003 [[1508.03172](#)].
- [34] G. H. Collin, C. A. Argüelles, J. M. Conrad and M. H. Shaevitz, *Sterile Neutrino Fits to Short Baseline Data*, *Nucl. Phys. B* **908** (2016) 354 [[1602.00671](#)].
- [35] S. Böser, C. Buck, C. Giunti, J. Lesgourgues, L. Ludhova, S. Mertens et al., *Status of Light Sterile Neutrino Searches*, *Prog. Part. Nucl. Phys.* **111** (2020) 103736 [[1906.01739](#)].
- [36] V. Brdar and J. Kopp, *An Altarelli Cocktail for the MiniBooNE Anomaly?*, [2109.08157](#).
- [37] S. N. Gninenko, *The MiniBooNE anomaly and heavy neutrino decay*, *Phys. Rev. Lett.* **103** (2009) 241802 [[0902.3802](#)].
- [38] M. Masip, P. Masjuan and D. Meloni, *Heavy neutrino decays at MiniBooNE*, *JHEP* **01** (2013) 106 [[1210.1519](#)].
- [39] Y. Bai, R. Lu, S. Lu, J. Salvado and B. A. Stefanek, *Three Twin Neutrinos: Evidence from LSND and MiniBooNE*, *Phys. Rev. D* **93** (2016) 073004 [[1512.05357](#)].
- [40] J. R. Jordan, Y. Kahn, G. Krnjaic, M. Moschella and J. Spitz, *Severe Constraints on New Physics Explanations of the MiniBooNE Excess*, *Phys. Rev. Lett.* **122** (2019) 081801 [[1810.07185](#)].
- [41] P. Ballett, S. Pascoli and M. Ross-Lonergan,  *$U(1)'$  mediated decays of heavy sterile neutrinos in MiniBooNE*, *Phys. Rev. D* **99** (2019) 071701 [[1808.02915](#)].
- [42] E. Bertuzzo, S. Jana, P. A. N. Machado and R. Zukanovich Funchal, *Dark Neutrino Portal to Explain MiniBooNE excess*, *Phys. Rev. Lett.* **121** (2018) 241801 [[1807.09877](#)].
- [43] C. A. Argüelles, M. Hostert and Y.-D. Tsai, *Testing New Physics Explanations of the MiniBooNE Anomaly at Neutrino Scattering Experiments*, *Phys. Rev. Lett.* **123** (2019) 261801 [[1812.08768](#)].
- [44] P. Ballett, M. Hostert and S. Pascoli, *Dark Neutrinos and a Three Portal Connection to the Standard Model*, *Phys. Rev. D* **101** (2020) 115025 [[1903.07589](#)].
- [45] O. Fischer, A. Hernández-Cabezudo and T. Schwetz, *Explaining the MiniBooNE excess by a decaying sterile neutrino with mass in the 250 MeV range*, *Phys. Rev. D* **101** (2020) 075045 [[1909.09561](#)].
- [46] A. de Gouvêa, O. L. G. Peres, S. Prakash and G. V. Stenico, *On The Decaying-Sterile Neutrino Solution to the Electron (Anti)Neutrino Appearance Anomalies*, *JHEP* **07** (2020) 141 [[1911.01447](#)].

- [47] M. Hostert and M. Pospelov, *Constraints on decaying sterile neutrinos from solar antineutrinos*, *Phys. Rev. D* **104** (2021) 055031 [[2008.11851](#)].
- [48] A. Datta, S. Kamali and D. Marfatia, *Dark sector origin of the KOTO and MiniBooNE anomalies*, *Phys. Lett. B* **807** (2020) 135579 [[2005.08920](#)].
- [49] W. Abdallah, R. Gandhi and S. Roy, *Understanding the MiniBooNE and the muon and electron  $g-2$  anomalies with a light  $Z'$  and a second Higgs doublet*, *JHEP* **12** (2020) 188 [[2006.01948](#)].
- [50] A. Abdullahi, M. Hostert and S. Pascoli, *A dark seesaw solution to low energy anomalies: MiniBooNE, the muon ( $g-2$ ), and BaBar*, *Phys. Lett. B* **820** (2021) 136531 [[2007.11813](#)].
- [51] B. Dutta, D. Kim, A. Thompson, R. T. Thornton and R. G. Van de Water, *Solutions to the MiniBooNE Anomaly from New Physics in Charged Meson Decays*, [2110.11944](#).
- [52] S. Vergani, N. W. Kamp, A. Diaz, C. A. Argüelles, J. M. Conrad, M. H. Shaevitz et al., *Explaining the MiniBooNE excess through a mixed model of neutrino oscillation and decay*, *Phys. Rev. D* **104** (2021) 095005 [[2105.06470](#)].
- [53] G. Karagiorgi, M. H. Shaevitz and J. M. Conrad, *Confronting the Short-Baseline Oscillation Anomalies with a Single Sterile Neutrino and Non-Standard Matter Effects*, [1202.1024](#).
- [54] J. Asaadi, E. Church, R. Guenette, B. J. P. Jones and A. M. Szelc, *New light Higgs boson and short-baseline neutrino anomalies*, *Phys. Rev. D* **97** (2018) 075021 [[1712.08019](#)].
- [55] H. Pas, S. Pakvasa and T. J. Weiler, *Sterile-active neutrino oscillations and shortcuts in the extra dimension*, *Phys. Rev. D* **72** (2005) 095017 [[hep-ph/0504096](#)].
- [56] D. Döring, H. Päs, P. Sicking and T. J. Weiler, *Sterile neutrinos with altered dispersion relations as an explanation for neutrino anomalies*, *Eur. Phys. J. C* **80** (2020) 1202 [[1808.07460](#)].
- [57] J. Kopp and J. Welter, *The Not-So-Sterile 4th Neutrino: Constraints on New Gauge Interactions from Neutrino Oscillation Experiments*, *JHEP* **12** (2014) 104 [[1408.0289](#)].
- [58] P. B. Denton, Y. Farzan and I. M. Shoemaker, *Activating the fourth neutrino of the  $3+1$  scheme*, *Phys. Rev. D* **99** (2019) 035003 [[1811.01310](#)].
- [59] G. A. Barenboim, P. Martínez-Miravé, C. A. Ternes and M. A. Tórtola, *Sterile neutrinos with altered dispersion relations revisited*, *JHEP* **03** (2020) 070 [[1911.02329](#)].
- [60] A. Y. Smirnov and V. B. Valera, *Resonance refraction and neutrino oscillations*, [2106.13829](#).
- [61] MICROBOONE collaboration, *Search for an Excess of Electron Neutrino Interactions in MicroBooNE Using Multiple Final State Topologies*, [2110.14054](#).
- [62] PARTICLE DATA GROUP collaboration, *Review of Particle Physics*, *PTEP* **2020** (2020) 083C01.
- [63] L. Wolfenstein, *Neutrino oscillations in matter*, *Phys. Rev. D* **17** (1978) 2369.
- [64] S. P. Mikheyev and A. Y. Smirnov, *Resonance Amplification of Oscillations in Matter and Spectroscopy of Solar Neutrinos*, *Sov. J. Nucl. Phys.* **42** (1985) 913.
- [65] V. Barger, K. Whisnant, S. Pakvasa and R. J. N. Phillips, *Matter effects on three-neutrino oscillations*, *Phys. Rev. D* **22** (1980) 2718.

- [66] A. Y. Smirnov, *The MSW effect and matter effects in neutrino oscillations*, *Phys. Scripta T* **121** (2005) 57 [[hep-ph/0412391](#)].
- [67] J. Linder, *Derivation of neutrino matter potentials induced by earth*, [hep-ph/0504264](#).
- [68] J. F. Nieves and S. Sahu, *Neutrino decoherence in an electron and nucleon background*, *Phys. Rev. D* **102** (2020) 056007 [[2002.08315](#)].
- [69] E. W. Kolb and M. S. Turner, *Supernova SN 1987a and the Secret Interactions of Neutrinos*, *Phys. Rev. D* **36** (1987) 2895.
- [70] S. Bilmis, I. Turan, T. M. Aliev, M. Deniz, L. Singh and H. T. Wong, *Constraints on Dark Photon from Neutrino-Electron Scattering Experiments*, *Phys. Rev. D* **92** (2015) 033009 [[1502.07763](#)].
- [71] COHERENT collaboration, *Observation of Coherent Elastic Neutrino-Nucleus Scattering*, *Science* **357** (2017) 1123 [[1708.01294](#)].
- [72] P. Coloma, M. C. Gonzalez-Garcia and M. Maltoni, *Neutrino oscillation constraints on  $U(1)'$  models: from non-standard interactions to long-range forces*, *JHEP* **01** (2021) 114 [[2009.14220](#)].
- [73] P. Ilten, Y. Soreq, M. Williams and W. Xue, *Serendipity in dark photon searches*, *JHEP* **06** (2018) 004 [[1801.04847](#)].
- [74] M. Fabbrichesi, E. Gabrielli and G. Lanfranchi, *The Dark Photon*, [2005.01515](#).
- [75] A. Caputo, A. J. Millar, C. A. J. O'Hare and E. Vitagliano, *Dark photon limits: A handbook*, *Phys. Rev. D* **104** (2021) 095029 [[2105.04565](#)].
- [76] P. Agrawal et al., *Feebly-interacting particles: FIPs 2020 workshop report*, *Eur. Phys. J. C* **81** (2021) 1015 [[2102.12143](#)].
- [77] MINIBoONE collaboration, *The MiniBooNE Detector*, *Nucl. Instrum. Meth. A* **599** (2009) 28 [[0806.4201](#)].
- [78] T2K collaboration, *Improved constraints on neutrino mixing from the T2K experiment with  $3.13 \times 10^{21}$  protons on target*, *Phys. Rev. D* **103** (2021) 112008 [[2101.03779](#)].
- [79] T2K collaboration, *Search for CP Violation in Neutrino and Antineutrino Oscillations by the T2K Experiment with  $2.2 \times 10^{21}$  Protons on Target*, *Phys. Rev. Lett.* **121** (2018) 171802 [[1807.07891](#)].
- [80] MINOS+ collaboration, *Precision Constraints for Three-Flavor Neutrino Oscillations from the Full MINOS+ and MINOS Dataset*, *Phys. Rev. Lett.* **125** (2020) 131802 [[2006.15208](#)].
- [81] NOvA collaboration, *An Improved Measurement of Neutrino Oscillation Parameters by the NOvA Experiment*, [2108.08219](#).
- [82] DAYA BAY collaboration, *Measurement of the Electron Antineutrino Oscillation with 1958 Days of Operation at Daya Bay*, *Phys. Rev. Lett.* **121** (2018) 241805 [[1809.02261](#)].
- [83] RENO collaboration, *Measurement of Reactor Antineutrino Oscillation Amplitude and Frequency at RENO*, *Phys. Rev. Lett.* **121** (2018) 201801 [[1806.00248](#)].
- [84] T2K collaboration, *Recent Results from T2K*, in *55th Rencontres de Moriond on Electroweak Interactions and Unified Theories*, 5, 2021, [2105.06732](#).
- [85] S. Gariazzo, C. Giunti, M. Laveder and Y. F. Li, *Updated Global 3+1 Analysis of Short-BaseLine Neutrino Oscillations*, *JHEP* **06** (2017) 135 [[1703.00860](#)].

- [86] M. Dentler, A. Hernández-Cabezudo, J. Kopp, P. A. N. Machado, M. Maltoni, I. Martinez-Soler et al., *Updated Global Analysis of Neutrino Oscillations in the Presence of eV-Scale Sterile Neutrinos*, *JHEP* **08** (2018) 010 [[1803.10661](#)].
- [87] A. Diaz, C. A. Argüelles, G. H. Collin, J. M. Conrad and M. H. Shaevitz, *Where Are We With Light Sterile Neutrinos?*, *Phys. Rept.* **884** (2020) 1 [[1906.00045](#)].
- [88] M. H. Moulai, C. A. Argüelles, G. H. Collin, J. M. Conrad, A. Diaz and M. H. Shaevitz, *Combining Sterile Neutrino Fits to Short Baseline Data with IceCube Data*, *Phys. Rev. D* **101** (2020) 055020 [[1910.13456](#)].
- [89] J. M. Berryman, P. Coloma, P. Huber, T. Schwetz and A. Zhou, *Statistical significance of the sterile-neutrino hypothesis in the context of reactor and gallium data*, [2111.12530](#).
- [90] B. Dasgupta and J. Kopp, *Sterile Neutrinos*, *Phys. Rept.* **928** (2021) 63 [[2106.05913](#)].
- [91] M. C. Gonzalez-Garcia, M. Maltoni and T. Schwetz, *NuFIT: Three-Flavour Global Analyses of Neutrino Oscillation Experiments*, *Universe* **7** (2021) 459 [[2111.03086](#)].
- [92] KAMLAND collaboration, *Reactor On-Off Antineutrino Measurement with KamLAND*, *Phys. Rev. D* **88** (2013) 033001 [[1303.4667](#)].
- [93] GALLEX collaboration, *Final results of the Cr-51 neutrino source experiments in GALLEX*, *Phys. Lett. B* **420** (1998) 114.
- [94] SAGE collaboration, *Measurement of the response of the Russian-American gallium experiment to neutrinos from a Cr-51 source*, *Phys. Rev. C* **59** (1999) 2246 [[hep-ph/9803418](#)].
- [95] J. N. Abdurashitov et al., *Measurement of the response of a Ga solar neutrino experiment to neutrinos from an Ar-37 source*, *Phys. Rev. C* **73** (2006) 045805 [[nucl-ex/0512041](#)].
- [96] F. Kaether, W. Hampel, G. Heusser, J. Kiko and T. Kirsten, *Reanalysis of the GALLEX solar neutrino flux and source experiments*, *Phys. Lett. B* **685** (2010) 47 [[1001.2731](#)].
- [97] C. Giunti, M. Laveder, Y. F. Li, Q. Y. Liu and H. W. Long, *Update of Short-Baseline Electron Neutrino and Antineutrino Disappearance*, *Phys. Rev. D* **86** (2012) 113014 [[1210.5715](#)].
- [98] V. Barinov and D. Gorbunov, *BEST Impact on Sterile Neutrino Hypothesis*, [2109.14654](#).
- [99] MINOS+ collaboration, *Search for sterile neutrinos in MINOS and MINOS+ using a two-detector fit*, *Phys. Rev. Lett.* **122** (2019) 091803 [[1710.06488](#)].
- [100] ICECUBE collaboration, *Searches for Sterile Neutrinos with the IceCube Detector*, *Phys. Rev. Lett.* **117** (2016) 071801 [[1605.01990](#)].
- [101] ICECUBE collaboration, *Searching for eV-scale sterile neutrinos with eight years of atmospheric neutrinos at the IceCube Neutrino Telescope*, *Phys. Rev. D* **102** (2020) 052009 [[2005.12943](#)].
- [102] V. V. Barinov et al., *Results from the Baksan Experiment on Sterile Transitions (BEST)*, [2109.11482](#).
- [103] C. Giunti, Y. F. Li, C. A. Ternes and Z. Xin, *Reactor antineutrino anomaly in light of recent flux model refinements*, [2110.06820](#).
- [104] RENO, NEOS collaboration, *Search for sterile neutrino oscillation using RENO and NEOS data*, [2011.00896](#).

- [105] NEOS collaboration, *Sterile Neutrino Search at the NEOS Experiment*, *Phys. Rev. Lett.* **118** (2017) 121802 [[1610.05134](#)].
- [106] RENO collaboration, *Spectral Measurement of the Electron Antineutrino Oscillation Amplitude and Frequency using 500 Live Days of RENO Data*, *Phys. Rev. D* **98** (2018) 012002 [[1610.04326](#)].
- [107] DAYA BAY collaboration, *Improved Measurement of the Reactor Antineutrino Flux and Spectrum at Daya Bay*, *Chin. Phys. C* **41** (2017) 013002 [[1607.05378](#)].
- [108] P. Huber, *NEOS Data and the Origin of the 5 MeV Bump in the Reactor Antineutrino Spectrum*, *Phys. Rev. Lett.* **118** (2017) 042502 [[1609.03910](#)].
- [109] V. Zacek, G. Zacek, P. Vogel and J. L. Vuilleumier, *Evidence for a 5 MeV Spectral Deviation in the Goesgen Reactor Neutrino Oscillation Experiment*, [1807.01810](#).
- [110] X. Qian and J.-C. Peng, *Physics with Reactor Neutrinos*, *Rept. Prog. Phys.* **82** (2019) 036201 [[1801.05386](#)].
- [111] DOUBLE CHOOZ collaboration, *Double Chooz  $\theta_{13}$  measurement via total neutron capture detection*, *Nature Phys.* **16** (2020) 558 [[1901.09445](#)].
- [112] A. C. Hayes, J. L. Friar, G. T. Garvey, G. Jungman and G. Jonkmans, *Systematic Uncertainties in the Analysis of the Reactor Neutrino Anomaly*, *Phys. Rev. Lett.* **112** (2014) 202501 [[1309.4146](#)].
- [113] D. A. Dwyer and T. J. Langford, *Spectral Structure of Electron Antineutrinos from Nuclear Reactors*, *Phys. Rev. Lett.* **114** (2015) 012502 [[1407.1281](#)].
- [114] P. Novella, *The antineutrino energy structure in reactor experiments*, *Adv. High Energy Phys.* **2015** (2015) 364392 [[1512.03366](#)].
- [115] A. C. Hayes and P. Vogel, *Reactor Neutrino Spectra*, *Ann. Rev. Nucl. Part. Sci.* **66** (2016) 219 [[1605.02047](#)].
- [116] M. Dentler, A. Hernández-Cabezudo, J. Kopp, M. Maltoni and T. Schwetz, *Sterile neutrinos or flux uncertainties? — Status of the reactor anti-neutrino anomaly*, *JHEP* **11** (2017) 099 [[1709.04294](#)].
- [117] C. Giunti, X. P. Ji, M. Laveder, Y. F. Li and B. R. Littlejohn, *Reactor Fuel Fraction Information on the Antineutrino Anomaly*, *JHEP* **10** (2017) 143 [[1708.01133](#)].
- [118] C. Giunti, *Statistical Significance of Reactor Antineutrino Active-Sterile Oscillations*, *Phys. Rev. D* **101** (2020) 095025 [[2004.07577](#)].
- [119] A. P. Serebrov, R. M. Samoilov and M. E. Chaikovskii, *Analysis of the result of the Neutrino-4 experiment in conjunction with other experiments on the search for sterile neutrinos within the framework of the  $3 + 1$  neutrino model*, [2112.14856](#).
- [120] MiniBooNE Collaboration, “Updated MiniBooNE neutrino oscillation results with increased data and new background studies (Version 1).” HEPData (collection), 2021.
- [121] MICROBOONE collaboration, *Search for an anomalous excess of inclusive charged-current  $\nu_e$  interactions in the MicroBooNE experiment using Wire-Cell reconstruction*, [2110.13978](#).
- [122] MICROBOONE collaboration, *Search for an anomalous excess of charged-current quasi-elastic  $\nu_e$  interactions with the MicroBooNE experiment using Deep-Learning-based reconstruction*, [2110.14080](#).

- [123] MICROBOONE collaboration, *Search for an anomalous excess of charged-current  $\nu_e$  interactions without pions in the final state with the MicroBooNE experiment*, [2110.14065](#).
- [124] C. A. Argüelles, I. Esteban, M. Hostert, K. J. Kelly, J. Kopp, P. A. N. Machado et al., *MicroBooNE and the  $\nu_e$  Interpretation of the MiniBooNE Low-Energy Excess*, [2111.10359](#).
- [125] P. B. Denton, *Sterile Neutrino Searches with MicroBooNE: Electron Neutrino Disappearance*, [2111.05793](#).
- [126] MicroBooNE Collaboration, “Search for an anomalous excess of charged-current quasi-elastic  $\nu_e$  interactions with the MicroBooNE experiment using Deep-Learning-based reconstruction (Version 1).” HEPData (collection), 2021.
- [127] MicroBooNE Collaboration, ““NuE simulation” of “Search for an anomalous excess of charged-current quasi-elastic  $\nu_e$  interactions with the MicroBooNE experiment using Deep-Learning-based reconstruction” (Version 1).” HEPData (dataset), 2021.
- [128] MicroBooNE Collaboration, ““NuE data and background (+ LEE) constrained prediction” of “Search for an anomalous excess of charged-current quasi-elastic  $\nu_e$  interactions with the MicroBooNE experiment using Deep-Learning-based reconstruction” (Version 1).” HEPData (dataset), 2021.
- [129] MicroBooNE Collaboration, “Search for an anomalous excess of inclusive charged-current  $\nu_e$  interactions in the MicroBooNE experiment using Wire-Cell reconstruction (Version 1).” HEPData (collection), 2021.
- [130] MicroBooNE Collaboration, ““ $\nu_e$ CC FC Energy Resolution” of “Search for an anomalous excess of inclusive charged-current  $\nu_e$  interactions in the MicroBooNE experiment using Wire-Cell reconstruction” (Version 1).” HEPData (dataset), 2021.
- [131] MicroBooNE Collaboration, ““ $\nu_e$ CC FC Efficiency” of “Search for an anomalous excess of inclusive charged-current  $\nu_e$  interactions in the MicroBooNE experiment using Wire-Cell reconstruction” (Version 1).” HEPData (dataset), 2021.
- [132] MicroBooNE Collaboration, ““Constrained  $\nu_e$ CC FC” of “Search for an anomalous excess of inclusive charged-current  $\nu_e$  interactions in the MicroBooNE experiment using Wire-Cell reconstruction” (Version 1).” HEPData (dataset), 2021.
- [133] R. Harnik, J. Kopp and P. A. N. Machado, *Exploring  $\nu$  Signals in Dark Matter Detectors*, *JCAP* **07** (2012) 026 [[1202.6073](#)].
- [134] D. G. Cerdeño, M. Fairbairn, T. Jubb, P. A. N. Machado, A. C. Vincent and C. Boehm, *Physics from solar neutrinos in dark matter direct detection experiments*, *JHEP* **05** (2016) 118 [[1604.01025](#)].
- [135] G. D. O. Gann, K. Zuber, D. Bemmerer and A. Serenelli, *The Future of Solar Neutrinos*, *Ann. Rev. Nucl. Part. Sci.* **71** (2021) 491 [[2107.08613](#)].
- [136] K. Goldhagen, M. Maltoni, S. Reichard and T. Schwetz, *Testing sterile neutrino mixing with present and future solar neutrino data*, [2109.14898](#).
- [137] J. R. Alonso et al., *IsoDAR@Yemilab: A Conceptual Design Report for the Deployment of the Isotope Decay-At-Rest Experiment in Korea’s New Underground Laboratory, Yemilab*, [2110.10635](#).
- [138] J. Alonso, C. A. Argüelles, J. M. Conrad, Y. D. Kim, D. Mishins, S. H. Seo et al., *Neutrino Physics Opportunities with the IsoDAR Source at Yemilab*, [2111.09480](#).